Investigations of p-type quantum dots in GaSb nanowires

Master thesis

Author: In-Pyo Yeo
30 hp, 1 year
Supervisors: Adam Burke and Sven Dorsch
Lund University

May 2021

LUND UNIVERSITY

FACULTY OF SCIENCE

Department of Physics
Division of Solid State Physics

Contents

Acknowledgment

I would like to thank both of my supervisors, Adam Burke and Sven Dorsch who were supervising my thesis for last two semesters. They have kindly helped me in every part of the thesis from the beginning to the end. It was a good chance for me to learn the techniques for both the fabrication and low temperature measurements of the quantum dot. They were also helping me a lot for writing skills in the thesis as well. And from this, I feel like my academic writing skills are fairly improved as for both in logical explanations of the outcomes and writing in English.

Abstract

The purpose of this project is to investigate hole transport in p-type quantum dots formed in GaSb nanowire and operating as single hole transistors. The individual and controlled hole-spin confinement in such system yields a variety of proposed applications for spintronics or quantum computation. In contrast to more conventional n-type material system, however, p-type quantum devices benefit from reduced hyperfine interaction, which are anticipated to result in longer spin lifetimes. One such p-type material system is GaSb, which to date has not been investigated in detail. This project starts with sample fabrication of p-type quantum dots in GaSb nanowires by the deposition of quantum dot island with Schottky contacts of nanowire segments combined with underlying metallic gate stripes. Transport characterization of the device properties are performed at low temperature.

The single quantum dot behaviour in different hole occupancy states is investigated by controlling the gate stripe potentials and the multi-quantum dot formation is also observed as well. Finally, via magneto-transport spectroscopy, the Zeeman effect is studied and g-factors of different orbital states are extracted with the measurement of spin-orbit interaction energy to be E_{so} = 113 μeV.

Acronyms

QD Quantum Dot

SQD Single Quantum Dot

DQD Double Quantum Dot

TQD Triple Quantum Dot

SET Single Electron Transistor

SHT Single Hole Transistor

SO Spin-Orbit

SD Source-Drain

BG Back Gate

SEM Scanning Electron Microscope

AC Acetone

IPA Isopropanol

EBL Electron Beam Lithography

US Ultra Sonic

PMMA Polymethylmethacrylate

MIBK Methyl Isobutyl Ketone

HCl Hydrogen Chloride

Ti Titanium

Au Gold

Ni Nickel

GS Ground State

ES Excited State

GaSb Gallium Antimonide

GaAs Gallium Arsenide

Si Silicon

InAsSb Indium Arsenide Antimonide

Ge Germanium

InSb Indium Antimonide

InAs Indium Arsenide

1 Introduction

A general definition of p-type quantum dot is the zero dimensional semiconductor material where the charge transport is dominated by holes [1]. The quantum dot is created when the size of the three dimensional bulk semiconductor material becomes smaller until the motion of charges are strictly confined in all three dimensions and the behaviour of hole transport through the quantum dot is measured by single hole transistor (SHT) device [2]. Studies of SHT based on p-type quantum dot in semiconductor nanowires is of increasing interest within the research field of quantum computation. The main principle for hole transport in SHT is followed by strong confinements of the quantum dot in low dimensional system. The binary digits of quantum computer, qubit is mainly operated by controlling the confined spins in the quantum dot and charge transport through tunnel barriers between two coupled single quantum dot (double quantum dots) [3]. Comparing with electron based spin by using n-type quantum dot, the hole based spin in p-type quantum dot materials are more beneficial to be used in quantum computation. This is because the electron-spin can interact with nuclei of quantum dot in semiconductor material (hyperfine interaction) which leads to a reduced life time [4]. In the case of hole-spins in p-type quantum dot, the hyperfine interaction is prevented since the hole wavefunction is built from p-orbitals and vanishing at nuclei positions [5]. Usually, the compound group III-V semiconductor (combination of group 3 and 5 elements in periodic table) with direct band gaps are used for quantum dot materials. These group III-V materials are inclined to have high mobility of charges and low excition binding energy [6]. And these properties are beneficial for group III-V materials to be applied into quantum computer in terms of the fast speed and strong confinements of charge carriers in the device [7] [8].

Nowadays, there are number of research studies for SHT reported based on several different p-type semiconductor materials such as Si, GaSb/InAsSb, GaAs and Ge and identifying its hole transport behaviour [9] [10] [11] [12]. However, there are few studies reported on pure GaSb due to the technological limitations for fabrication of small size quantum dot by Schottky contact between nanowire and metal gate electrode [13]. According to the previous research, the conductance of SHT for GaSb nanowire fabricated from heterostructure of GaAs/GaSb was measured and one obtains the high electrical conductance by I-V characteristics on the device both at room temperature 300 K and low temperature 1.5 K. These results shows that GaSb can be possible to become another prominent candidates for quantum computation technology [14].

The aim of this project is to investigate the formation of quantum dots in Schottky-contacted GaSb nanowires combined with bottom gate arrays. The experiments start with the fabrication of GaSb quantum dot in the cleanroom laboratory. And the measurements of hole transport in quantum dot is performed at low temperature by using an Oxford Instruments Triton 200 dry dilution refrigerator. The main research question in this project is to identify the hole transport behaviour in quantum dot in GaSb nanowire and whether it follows the same behaviour as other p-type materials or if there is any differences found which can be distinguished with them. In general, the SHT are inclined to have clear single quantum dot behaviour at higher occupancy hole regime but turning into double quantum dot in lower oc-

cupancy hole regime due to the roughness of valence band edge in potential well and this is clearly resolved in p-type Si quantum dot [9]. Another important factor which needs to be considered in this project is finding spin-orbit interaction energy of the quantum dot in GaSb nanowire. This is because the life time of spin-qubit in quantum computer is highly dependent on its spin-orbit interactions [15]. One of the main limitations in this project is the low current measurements as the conductance current is in pA scale. Another limitation is the risk of large quantum dot formation by Schottky contact with GaSb nanowire since one expects to create small size of quantum dot in strong quantum confinements.

These are the reasons why one study how the bottom gate arrays can be used to form reliable quantum dots in GaSb. Based on knowledge gained by doing so, one is able to tune a device into a SHT regime and study the magneto-transport properties.

The part of results in this project is being published in the paper and uploaded on arXiv [13].

2 Theory

2.1 Semiconductor material

In this project, the GaSb nanowires in p-type extrinsic semiconductor is investigated. This extrinsic semiconductor is more beneficial to be used in various technological applications such as quantum computations due to the higher charge conductivity than intrinsic semiconductor. This section initiates with the backgrounds of both intrinsic and extrinsic semiconductors.

The differences of solid materials, metal and semiconductor is usually distinguished by electron filled states in energy band and the positions of chemical potential, μ (Fermi energy level, E_F) at zero temperature, T = 0 K. The semiconductor has normally poor electrical conductivity compared with metal and this is explained in Fig.1 in terms of density of total number of electron occupied states $f(E_F, T)g(E)$ where $f(E_F, T)$ is the Fermi dirac distribution function and $g(E)$ is the density of states [16].

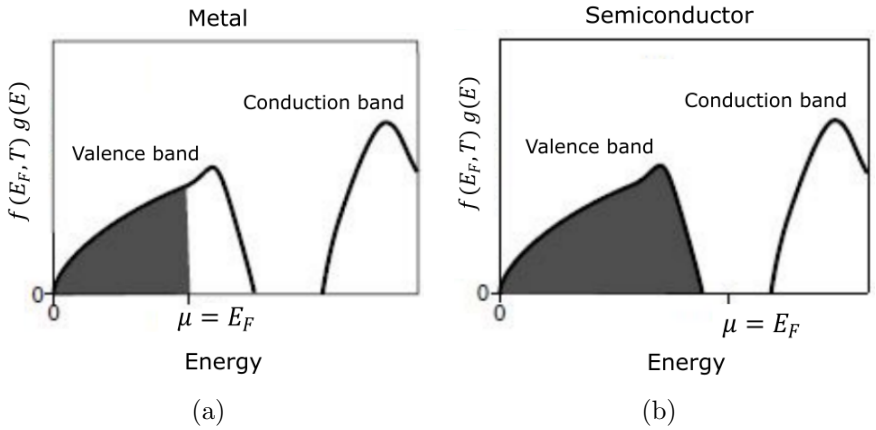

Figure 1: The density of electronic occupied states for both (a) metal and (b) semiconductor (Figure adapted from [16])

Figure 1 (a) indicates how the electron is filled in the energy band for metal and (b) is for semiconductor. As for the semiconductors, all states are filled far below chemical potential, μ. However in metals, the states are still available right above the Fermi energy hence, metals are highly conductive. In other words, the transport of electrons requires the available states, which means that electrons are possibly to be excited close to μ where there are many available states in metal energy band and this determines high electrical conductivity of metal. On the other hand, the electrons are completely filled up to band gap (energy differences between lowest edge of the conduction band and highest edge of the valence band) for semiconductor and this makes it hard for electrons to be excited into conduction band due to the band gap which results in poor electrical conductivity compared with metal. And this kind of semiconductor as illustrated in Fig.1 is called 'intrinsic semiconductor' where its chemical potential at 0 K is located on energy where its density of states is 0 and one of the energy band is entirely filled and other band is empty [16][17].

The electrons are distributed according to the Fermi-Dirac distribution by Pauli exclusion for fermions where its occupation states should be either 0 or 1 at 0 K as

shown in Fig.2.

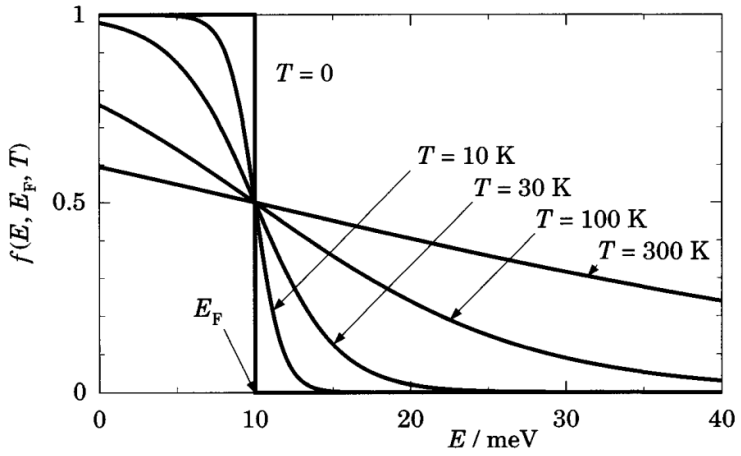

Figure 2: The Fermi-Dirac distribution function at different temperature in the fixed chemical potential, E_F=10 meV (Figure adapted from [18])

The Fermi Dirac distribution function, $f(E, E_F, T)$ represents the probability of electron states being occupied at finite temperature, T and Fermi energy level, E_F in the system. As it is shown in Fig.2, the function takes solutions in between 0 and 1 where the all curves for different temperatures intersect at $f(E, E_F, T) = 0.5$ and there is a 50% probability of the state energy being occupied or empty for all different temperatures when $E = E_F$. The transition between occupation states 1 to 0 (f=1 $\rightarrow$ f=0) becomes broader as the temperature rises. At low temperature approximately T=0 K, the Fermi-Dirac distribution becomes step-like function where the all of states are entirely occupied at $E < E_F$ and empty at $E > E_F$. These relations of temperature dependence of Fermi dirac distribution function is expressed by

$$f(E, E_F, T) = [\exp(\frac{E - E_F(T)}{K_B T}) + 1]^{-1} \tag{1}$$

where k_B is the Boltzmann's constant and the width of function is changed exponentially depending on finite temperature as shown in Fig.2 [18].

These temperature effects cause changes of electron filling states in the energy band of the intrinsic semiconductor. Figure 3 shows how the electrons are excited from valence band and added into conduction band at finite temperature $T > 0$ K.

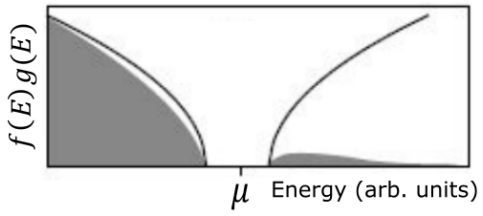

Figure 3: An intrinsic semiconductor and how its filled state is affected by the finite temperature (Figure adapted from [16])

As it is shown in Fig.3, the valence band becomes partially filled as the number of electron occupied states are populated into conduction band at finite tempera-

ture. And, this results in an increase of the conductivity of solid since the electron transports are available into the empty states in valence band [16].

2.1.1 Extrinsic semiconductor

The intrinsic semiconductor is difficult to be used for technological applications because of its low conductivity. In order to solve this problem, one can add impurities to turn it into an extrinsic semiconductor and this process is called 'doping'. The doping changes an electrical conductivity of the semiconductor by either increasing number of electrons or holes depending on which types of impurities are added [19]. Figure 4 below indicates how the compound intrinsic semiconductor Gallium Antimonide (GaSb) becomes extrinsic by either donating or accepting electrons.

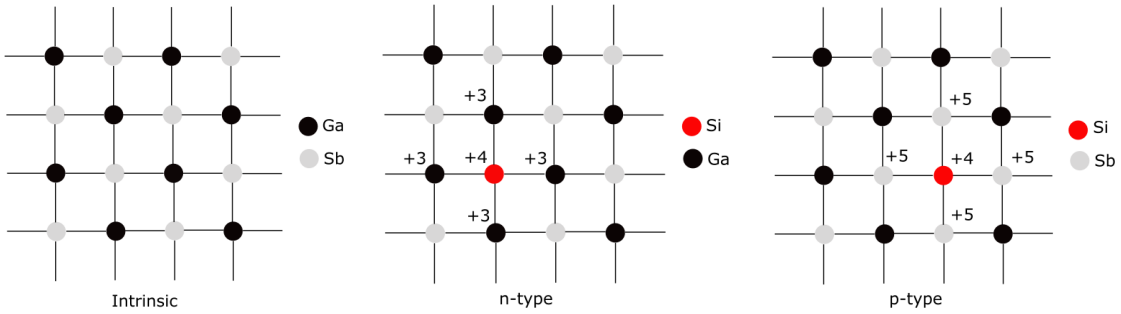

(a) (b) (c)

Figure 4: An example of intrinsic semiconductor, GaSb (a) and how it becomes different types of extrinsic n-type (b) and p-type (c) depending on whether the dopant accepts or donates free electrons

The dopant impurity atom usually comes from the group 13 or 14 elements in the periodic table depending on how they form the covalent bond with atoms. Figure 4 (b) shows how the donor-doped (n-type) semiconductor is produced by replacing one of the Sb atoms with a Silicon (Si) impurity atom . The Ga is the element on group 13 in periodic table which has 3 valence electrons and the Si is on group 14 with 4 valence electrons. This results in one extra conduction electron among the covalent bonds between two atoms. Therefore, a semiconductor where its majority charge carrier is electron is created and this is called n-type semiconductor. Similarly, a acceptor doped (p-type) semiconductor is produced if the impurity atom with less number of valence electron than covalently bonded atoms is added. In this case, the Ga atom is switched into Si and forms the covalent bonds with Sb atoms as shown in Fig.4 (c). The positively charged hole is created while one extra electron is accepted into Si atom since Sb atom is the element on group 15 with 5 valence electrons. In other words, the majority charge carrier in p-type semiconductor is hole rather than electron [1].

An energy band diagram for how the both n-type and p-type semiconductor is different with intrinsic semiconductor is given in Fig.5.

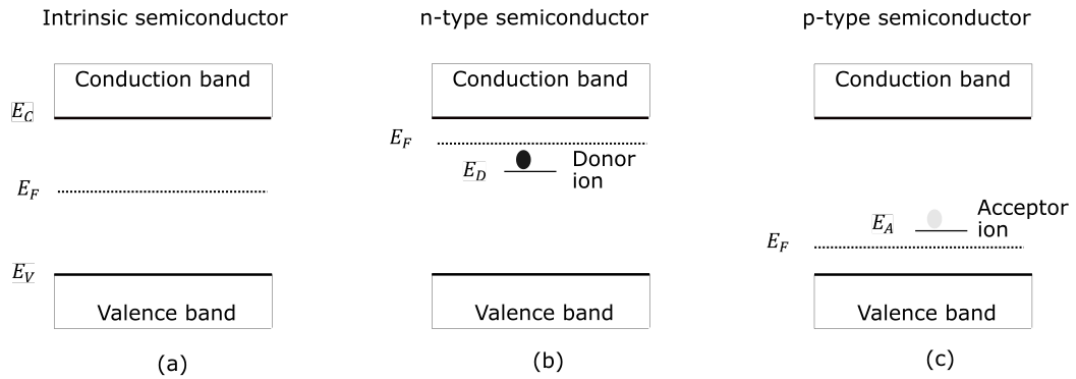

Figure 5: (a) An energy band diagram of intrinsic semiconductor and how both n-type (b) and p-type (c) semiconductor are created depending on their ionized ions

As for the intrinsic semiconductor, the Fermi energy, E_F is near to the middle of band gap. The Fermi energy is shifted nearer to the conduction band in n-type semiconductor. There is also an additional ionized donor level E_D which is created below the Fermi energy at finite temperature and there are many of the donor ions distributed on the level. These donor ions donate the electrons on the conduction band where the majority charge carriers becomes electron. On the other hand, the Fermi energy is closer to the valence band in p-type semiconductor. The ionized acceptor level E_A is created above the Fermi energy and they accept electrons from the valence band with leaving holes where the majority charge carriers becomes holes in this case. [20].

2.1.2 p-type Schottky barrier

The Schottky contact is fabricated when the thin metallic electrode is deposited on the surface of semiconductor with low-doped concentration [21]. In this project, the Schottky contact is used to fabricate the quantum dot island on the barrier formed by GaSb nanowire segments and metallic electrodes. A p-type Schottky barrier is defined as the work function created by energy differences between metal Fermi energy level and the valence band edge of the p-type semiconductor on the contact interface [21]. The formation of Schottky barrier is mainly caused by work function mismatching, the balancing Fermi energy levels for both metal and semiconductor at thermal equilibrium and continuity of vaccum energy level, E_{vac} [22]. Figure 6 below shows a band diagram of how the Schottky barrier is formed when the p-type semiconductor has a contact with surface of metal.

The barrier height work function, $q\varphi_p$ is calculated by

$$q\varphi_p = E_p + qV_d \tag{2}$$

where E_p is the energy differences between edge of the valence band and Fermi energy level and qV_d is the work function for built-in potential and in this case, a charge transfer is blocked by the barrier [23]. The Schottky barrier is usually formed at condition in low doping concentration of semiconductor material. If the doping concentration becomes higher, it loses the behaviour of Scottky contact and turning into quasi-ohmic contact. In this case, a contact resistance becomes negligible compared with series or bulk resistance of semiconductor which makes the barrier height low enough that electron can pass through the barrier [22].

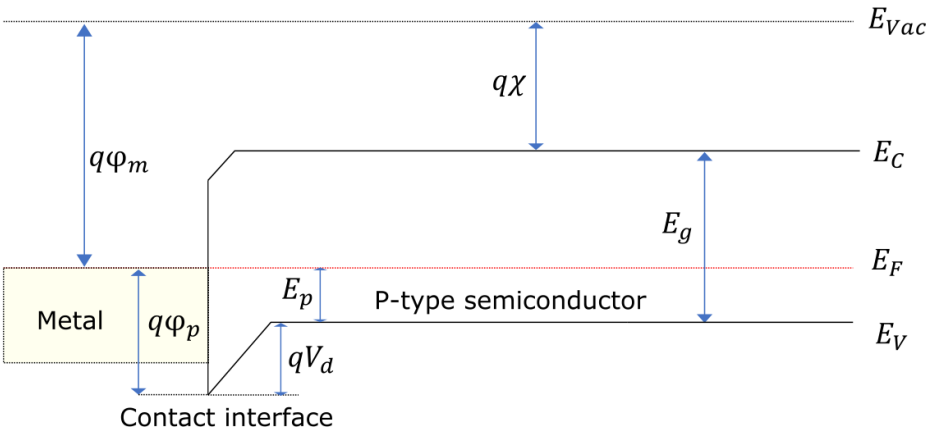

Figure 6: An illustration of p-type Schottky barrier with different work functions where $q\varphi_m$ is the metal, $q\chi$ is the electron affinity, $q\varphi_p$ is the barrier height and qV_d is the built-in potential

2.1.3 Group III-V materials

A group III-V material is the compound semiconductor where it consists of group 13 elements (B, Al, Ga, In, Tl) and group 15 anions (N, P, As, Sb, Bi) in periodic table [24]. Figure 7 below shows the lattice constants mismatches and how the band gap varies with different compound semiconductors compositions (lines connecting the pure elements).

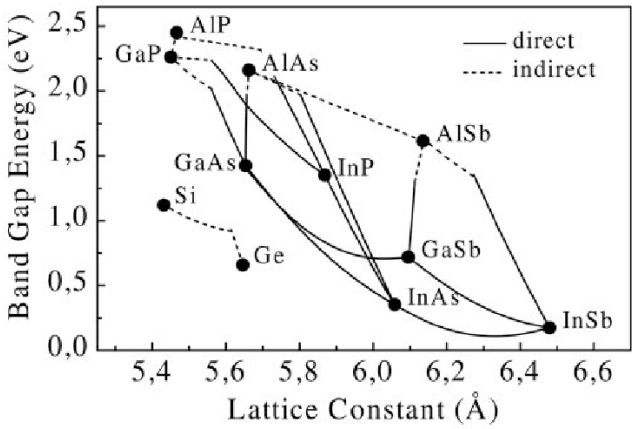

Figure 7: An illustration of group III-V material with lattice constants and band gap energies (Figure adapted from [25])

As it is shown in Fig.7, the compound semiconductors are inclined to have direct band gap at large lattice constant and small band gap energy (InP, GaAs, GaSb, InAs and InSb). These III-V materials with direct band gap are the candidates for high performance optoelectronics device since the photon emission in direct band gap is more efficient than indirect band gap in respect to conservation of both energy and momentum [26].

Another property of group III-V materials is the high mobility of charge carriers and low exciton binding energy which determines how fast charges are free to move inside of semiconductors [6]. And, these features make them available to be used in other technological applications, spintronics and quantum computation where its

principle of information processing is based on electron/hole spin confinements in quantum dot. The high mobility of charges determine the faster computation speed by the binary digits, spin-qubits and the low exciton binding energy decides the strong quantum confinements of individual electron/hole states in quantum dots [7][8]. And, the performance of devices is highly dependent on long life time of its spin states. However, there is one disadvantage of using electron spin based quantum dot in n-type semiconductor materials, since the electrons can interact with nuclei in quantum dot (hyperfine interaction) which leads to relaxation and decoherence of excited spin states. Therefore, it is more beneficial to use hole spin based quantum dot as the hole states are initially created from p-orbital that goes to zero at nuclei and this prevents the hyperfine interaction [5]. These group III-V materials are applied into quantum computation research and the GaSb is considered to be another interesting candidate according to the high hole mobility of quantum device [27]. However, there is limited number of relevant experimental data reported about spin transport behaviour on p-type GaSb quantum devices yet according to technological issues on fabrication and growth process of nanostructured devices. According to the previous research, a hole transport of GaSb was investigated with the fabrication process of device from GaAs/GaSb heterostructure nanowires [14]. The high conductance of device was measured as I-V characteristics of ohmic behaviour for both at room temperature 300 K and low temperature 1.5 K. The preliminary results showed that the GaSb has potential to become another prominent candidate for quantum information technology by spin such as quantum computing where each quantum mechanical binary digit, qubit is controlled by spin of the excess charge carriers on single electron/hole quantum dot [14][3].

2.2 Quantum dot

A quantum dot is an artificial made material in low dimensional system where the motion of charge is confined in three dimensions. The artificial atom is defined as small boxes containing a semiconductor material where the electrons are trapped inside [28]. Unlike with natural atoms, where its central position is filled by positive nucleus, the artificial atom contains potential well where the electrons are confined in the quantized energy level on the well. The measurements of conductance in artificial atom is done with a current or voltage through the separated tunnel barriers in quantum dot which is coupled into electrical leads and this principle can be reflected into Single Electron Transistor (SET) which is described in the next section 2.2.1 [29][28]. The materials are usually classified into bulk and low dimensional system depending on restriction of motion of the charges in one or more directions due to quantum confinement effect. An illustrations of materials in each dimension systems is shown in Fig. 8 where the magnitude of confinement dimension for the charge with its De-broglie wavelength sets to be order of 10 nm scales in order to make systems to be confined and observe the quantization effects [30]. In bulk materials, the charge carriers are free to move in three dimensions which is denoted as three dimensional (3d) system. A quantum well is an example of two dimensional (2d) system where charge carriers can freely move in two dimensions but confined in one dimension. A quantum wire is an one-dimensional (1d) system since the carriers are confined in two dimension and only free to move in one dimension. On the other hand, charge carriers in quantum dots are tightly confined in three dimension, referred as zero

dimensional (0d) system and in this case, discrete energy levels are quantized in all three directions and the energy of conduction electrons in the system, E_{n_x,n_y,n_z} can be written as [2]

$$E_{n_x,n_y,n_z} = \frac{h^2\pi^2}{8m^*}\left(\frac{n_x^2}{L_x^2} + \frac{n_y^2}{L_y^2} + \frac{n_z^2}{L_z^2}\right) \tag{3}$$

where m* is the effective mass of electron, h is the planck constant, n_x, n_y and n_z are quantum numbers, L_x, L_y and L_z are dimensions in each axis and this expression in Eq. 3 is only suitable for particle in a box model referred as infinite potential well in 3d system. This system can be applied into this project if the fabricated quantum dot islands forms the parabolic potential well.

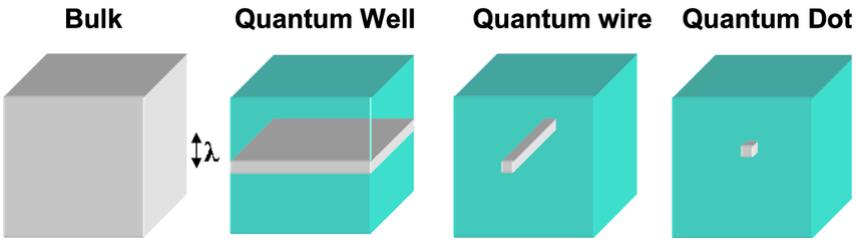

Figure 8: A diagram of bulk and low dimensional nanostructured materials in different confinement systems where λ denotes the De broglie wavelength where its magnitudes are in the order of confinement dimensions (Figure adapted from [30])

2.2.1 Single hole transistor (SHT)

A Single hole transistor is one of the technological applications of quantum dots where major charge carrier transported through the quantum dot is hole. However, its theory and principle of SHT is able to be reflected and described by single electron transistor (SET) where the charge carrier is switched into electron rather than hole.

A SET is solid state device containing an integer number of electrons trapped in the device which consists of small island of quantum dot. This island forms a discrete quantized energy level inside and its eigenstates are filled by electrons [31]. These electrons in quantum dot island are transferred through separated tunnel barriers connected into electrode reservoirs and the basic schematic illustration of this SET is illustrated in Fig. 9. As it is shown in Fig. 9, a quantum dot is tunnel coupled into source and drain reservoirs through two separated tunnel barriers connected to edges of quantum dot. In this region, there is an exchange of electrons between two reservoirs by quantum tunneling effect. There is a gate electrode also capacitively connected into quantum dot and this controls the condition of electrostatic potential of quantum dot in response to connected reservoirs [31].

The electronic behavior of the SET is determined by the Coulomb blockade effects. This is caused by two electrons repelling (Coulomb repulsion) inside of quantum dot and this blocks the current flowing on the system. The number of electrons in the quantum dot can be controlled by charging an additional electron on the island by tuning the gate electrode. This additional electron makes a change of

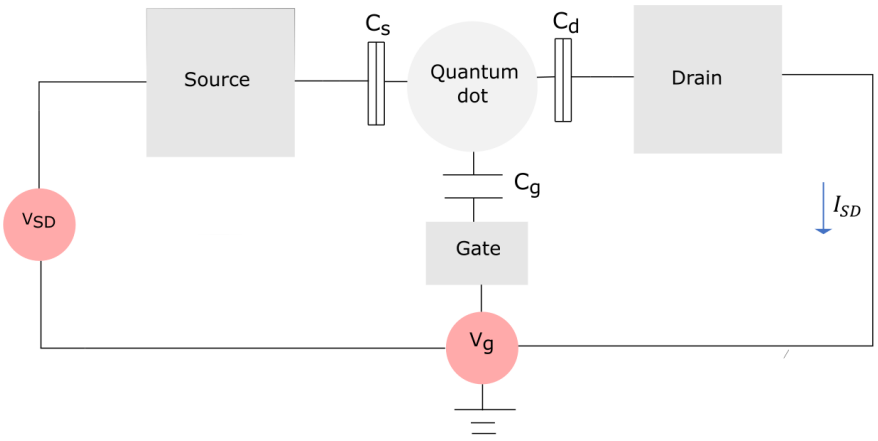

Figure 9: An illustrations of SET made up of electrode components tunnel coupled into quantum dot. The current, I_{SD} is flowing through the device and measured with regards to gate, V_g and bias, V_{SD} voltages while electron is transported through the quantum dot which is coupled with source and drain reservoirs through separated tunnel barriers

electrostatic potential of the island by charging energy ($E_c = e^2/C$, where C is the self capacitance of the quantum dot) which is defined as energy differences between two successive electrons on the quantum dot and this requires a condition of small source-drain bias and low temperature ($E_c > k_BT$, where k_B is the boltzmann constant) [32].

2.2.2 Transport across quantum dots

Consider the SET model in Fig.9 where the quantum dot island is connected to both V_{SD} and V_g capacitively. If the external charge, Q_{ext} is induced on the island by tuning the gate electrode, the electrostatic potential differences between quantum dot and electrode reservoirs is found as [33]

$$\phi(Q) = Q/C + \phi_{ext} \tag{4}$$

where Q is the induced charges on the quantum dot island due to the electrostatic potentials on gate and source and drain electrodes, ϕ_{ext} is the electrostatic potential differences by induced external charge and C is the sum of total capacitances connected on the electrodes ($C = C_s + C_d + C_g$). A total electrostatic energy of the island can be derived from integration of the potential by charge,

$$U(N) = \int_0^{-Ne} \phi(Q')\, dQ' = \frac{(Ne)^2}{2C} - Ne\phi_{ext} \tag{5}$$

where N is the total number of induced charges on the island ($Q = Ne$, where N is the integer number of charge) and the expression on Eq.5 can be rewritten into

$$U(N) = \frac{(Ne - Q_{ext})^2}{2C} - \frac{Q_{ext}^2}{2C} \tag{6}$$

The quantum dot island has discrete energy levels and the electron occupation probability on the level of the quantum dot depends on its energetic positions, the tunnel couplings and the Fermi-Dirac distributions of the contacts

The energy diagram of the SET where the tunnel barriers are coupled with source and drain electrode reservoirs is illustrated in Fig.10. At low temperature, the electrode reservoirs are filled with electrons up to both chemical potentials of source, μ_s and drain, μ_d by Fermi-Dirac distribution. If the small external bias, V_{SD} is applied, both μ_s and μ_d are shifted and a transport window is opened in the region which is created by potential differences between source and drain chemical potentials, $V_{SD} = (\mu_s - \mu_d)/e$.

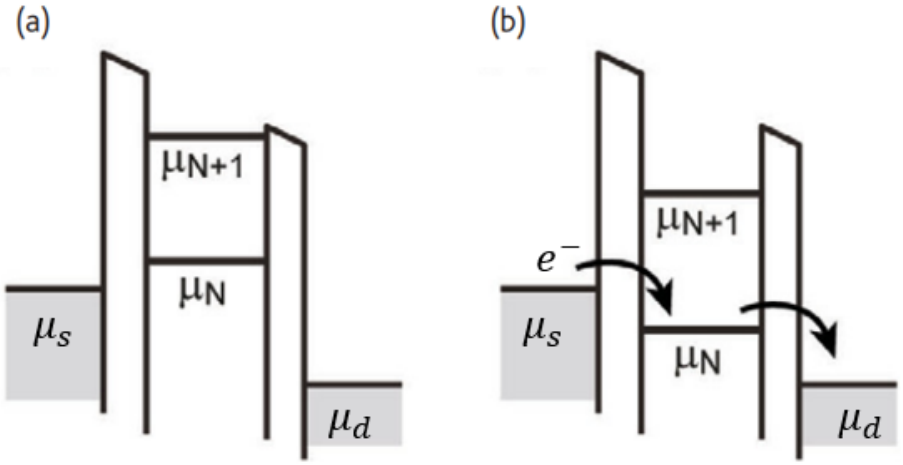

Figure 10: (a) A band diagram of the SET with electrons confined between tunnel barriers. (b) An electron transports through the transport window in tunnel barrier with increasing gate voltage, V_g (Figure adapted from [34])

Figure 10 indicates how the electron tunnels through the SET while applying V_{SD} where the electrons are spatially confined between tunnel barriers which are coupled to source and drain reservoirs. The chemical potential of the quantum dot island μ_N which indicates the energy required to add the N_{th} electron on the system and this can be calculated by taking the differences between electrostatic energy of N and $N-1$ electron states on quantum dot at low temperature as [32]

$$\mu(N) = U(N) - U(N-1) \tag{7}$$

The electrons can only be transported through the tunnel barrier if the chemical potential of an island is located inside of the transport window as shown in Fig.10 (b). By inserting the expression of U_N obtained from Eq.5 into Eq.7, μ_N can be revealed in terms of capacitances and gate voltage. Therefore, the chemical potential in the island for N electrons on the quantum dot is re-expressed as

$$\mu(N) = \epsilon_N + \frac{(N - N_0 - 1/2)e^2}{C} - e\frac{C_g}{C}V_g \tag{8}$$

where ϵ_N is the single particle energy level and N_0 is the number of background charges remaining on quantum dot at $V_g = 0$ V. The ratio of gate capacitance, C_g and total capacitance, C is defined as lever arm, $\alpha_i = -\frac{C_g}{C}$ [35]. The change in V_g shifts down the chemical potential of an island, μ_N and this determines whether an electron is transported or blocked in the quantum dot.

As it is mentioned above, a transport window is opened if the μ_s and μ_d is shifted while applying small source-drain bias, V_{SD}. Consider an initial situation where the energy level is out of the transport window at $V_g = 0$. And, the electron can only transport into quantum dot if the chemical potential of an island for electron states are located inside of the transport window. If the small positive V_g starts being applied, the chemical potential of N electron state in island is shifted down and electron from the source can jump into drain through the tunnel barrier of quantum dot since its energy level comes inside of transport window. However, the electron transport is blocked if more positive V_g is applied that its energy levels moves down to bottom of the μ_d (outside of the transport window). In order to make the system to flow current again, next electron state of chemical potential, $N + 1$ should be brought down into transport window by applying more V_g and shifts down next energy levels. An energy difference between two chemical potential of the electron states ($N + 1$ and N) is defined as addition energy as

$$\mu_{N+1} - \mu_N = \Delta\epsilon_N + \frac{e^2}{C} \tag{9}$$

The second term is defined to be charging energy, $\frac{e^2}{C} = E_c$ and this energy should be added into system to bring down the next energy level into transport window by tuning the V_g. The first term $\Delta\epsilon_N$ is the single particle energy level differences in orbital state and this will be more discussed in section 2.3.2.

These patterns of Coulomb blockade illustrate whether electrons are transported or blocked inside of the quantum dot and can be analyzed by two different ways. The first method is to detect the conductance of Coulomb peaks by sweeping only gate voltage V_g with fixed set of source-drain bias, V_{SD}. The second method is to build the two dimensional conductive regions in V_{SD}-V_g plane by sweeping both V_g and V_{SD} at certain range and they are illustrated in Fig. 11 (b).

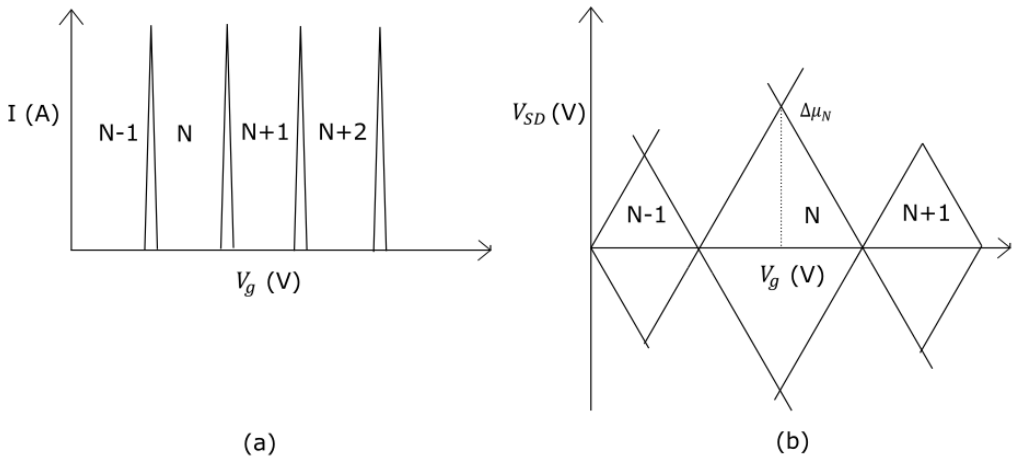

Figure 11: (a) A periodic coulomb oscillation of conductance peaks where electron is transported or blocked (b) A charge stability diagram as a function of gate voltage and source-drain bias. An electron transport is blocked inside of the Coulomb diamond

As it is shown in Fig.11 (a), one can measure the periodic oscillation of conductance (Coulomb) peaks while sweeping the V_g. These are the points where the chemical

potential of number of electron states are in transport window as the electron is added so the current can be flowing as described in Fig.10 (b). The region between two conductance peaks are the coulomb blockade region where the electron transport is blocked since the chemical potential of an island is out of the transport window in this case. Figure 11 (b) shows the charge stability diagram built in the plane of V_{SD} and V_g with the formation of diamond shaped patterns (Coulomb diamond). The electron transport is blocked inside of the area of Coulomb diamond which is referred as Coulomb blockade and the current is flowing only outside of the diamond region. The addition energy, $\Delta\mu_N$ can be calculated by measuring the height of the Coulomb diamond and the coulomb peaks observed in (a) matches with intersection points of Coulomb diamonds on horizontal axis, V_g where the electron states are added.

2.3 Applying external magnetic field on quantum dot

2.3.1 Spin-Orbit interactions on electrons

The spin-orbit interaction energy is important to be considered to determine the confinements of hole-spin states in quantum dot. A spin is defined as the intrinsic angular momentum of electron and it was first introduced in order to explain how a magnetic field interacts with electron magnetic moment and identifying angular momentum of electronic motion. This interaction causes the multiple splittings of spectral lines which is called the Zeeman effect and this will be more discussed in section 2.3.3. A derivation of spin-orbit interaction energy in one electron system is followed by the book 'Spectrophysics : Principles and Applications' written by A. Thorne [36]. The spin on the atomic energy level follows the principle of classical electrodynamics for rotating charged body where the angular momentum of rotating spin, $\vec{s}$ creates a magnetic moment, $\vec{\mu}$ on the axis [36]

$$\vec{\mu} = \frac{q}{2m}\vec{s} \tag{10}$$

where q is the electric charge and m is the mass of the charged body. Equation 10 can be rewritten as the electron spin magnetic moment in terms of the Bohr magneton, $\mu_B = e\hbar/2m_e$ and the gyromagnetic ratio of electron, g_s

$$\vec{\mu_s} = -g_s\frac{\mu_B}{\hbar}\vec{s} \tag{11}$$

The spin-orbit interaction can be identified by interaction of spin magnetic moment with magnetic field, $\vec{B_l}$ created by moving nucleus which is proportional to orbital angular momentum, $\vec{l}$

$$E_{so} = -\vec{\mu_s}\cdot\vec{B_l} = C\cdot\vec{l}\cdot\vec{s} \tag{12}$$

where C is the proportionality constant and the spin orbit interaction energy, E_{so} is dependent on scalar product of spin and orbital angular momentum, $l\cdot s$. The magnitude of l and s are constant, however its vector orientations are changed by interactions between angular momentum as shown in Fig.12

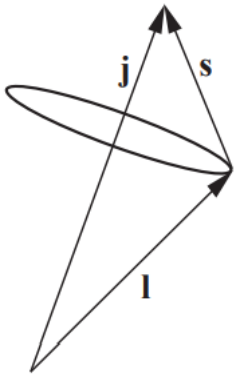

Figure 12: A vector model of spin and orbital angular momentum with its precession of total angular momentum of electron in spin-orbit interaction (Figure adapted from [37])

The total angular momentum $\vec{j}$ is calculated by adding spin and orbital angular momentum.

$$\vec{j} = \vec{l} + \vec{s} \tag{13}$$

The sum of two angular momentums is constant if there is no external torque applied on the system. The interaction between the spin and orbital angular momentum causes their vectors to precess around the direction of total angular momentum j as shown in Fig.12. The scalar product of $\vec{l} \cdot \vec{s}$ is expressed in terms of $\vec{j}$, $\vec{l}$ and $\vec{s}$ by using the relation, $\vec{j}^2 = \vec{l}^2 + \vec{s}^2 + 2\vec{l} \cdot \vec{s}$ as

$$\vec{l} \cdot \vec{s} = \frac{1}{2}(\vec{j}^2 - \vec{l}^2 - \vec{s}^2) \tag{14}$$

Finally, the energy of spin orbit interaction can be calculated by inserting Eq.14 into Eq.12 above and introducing a constant splitting factor, $\zeta_{nl} = \frac{R\alpha^2 Z^4}{n^3 l(l+\frac{1}{2})(l+1)}$

$$E_{so} = \zeta_{nl} \frac{1}{2}(j(j+1) - l(l+1) - s(s+1)) \tag{15}$$

where the numerical constant value of $R\alpha^2 = 5.843$ cm^{-1}, α is the fine structure constant as $\alpha = \frac{e^2}{4\pi\epsilon_0 \hbar c}$, n is the principal quantum number and Z is the atomic number.

2.3.2 Spin filling states in quantum dot

In quantum mechanics, an energy level becomes degenerate if there is more than one measurable state providing an equal value of energy at the same quantum number. The filling of spin in the quantum dot while adding an additional electron to the system follows the Pauli exclusion principle where the total number of spin should be either $S = 0$ or $S = 1/2$ in the state [31]. This is because a single electron state in the quantum dot has either two-fold or higher degeneracy which contains two single-particle energy levels in each state ($\epsilon_1 = \epsilon_2$) and the order of alternating spin is filled in the state when the electron is added and this is illustrated in Fig.13.

As it is shown in Fig.13 (a), there are two degenerate single particle energy levels in each quantized energy level of quantum dot island ($\epsilon_1 = \epsilon_2$), ($\epsilon_3 = \epsilon_4$) and ($\epsilon_5 = \epsilon_6$). The alternating spin is filled in each single-particle energy level as the next electron is added. And this determines the addition energy of the quantum dot. In the previous section, one derived the addition energy as $\Delta\mu_N = \Delta\epsilon_N + \frac{e^2}{C}$ where the first term is the single-particle energy level differences and second term is the charging energy. If the second electron is added into the island, the addition energy from the first electron state is equal to the charging energy since there is no change of single particle energy level. However, if the third electron is added, one should include the energy level differences since $\epsilon_3 \neq \epsilon_2$ where the addition energy becomes larger than charging energy and this is illustrated in Fig.13 (b).

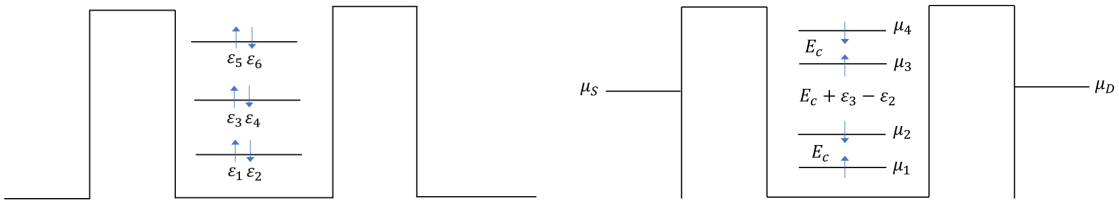

(a) (b)

Figure 13: (a) The spin fillings in two-fold degenerate of single electron with single-particle energy levels in quantum dot island. (b) The change of addition energy in quantum dot island depending on single particle energy level

2.3.3 Zeeman effect

A Zeeman effect is the splitting of energy level of total angular momentum, j when the weak external magnetic field, B interacts with atom. This is caused by breaking the degeneracy of spin and orbital states as the magnetic field changes the motion of magnetic moment and angular momentum of both spin and orbital states and makes them precessing around the field axis [38]. In the quantum dot, the external magnetic field breaks the spin degeneracy and splits both of the ground and excited states of the orbital states and this is illustrated in Fig.14.

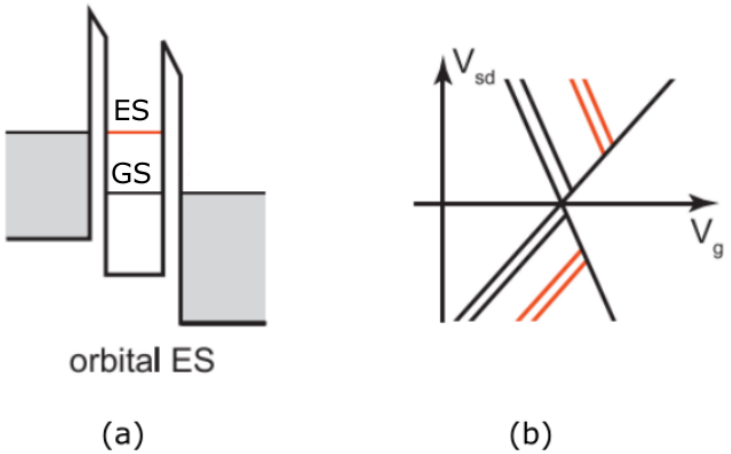

(a) (b)

Figure 14: (a) The ground (GS) and excited (ES) states of orbital in quantum dot. (b) The Zeeman splitting of both GS and ES of orbital states (Figure adapted from [39])

As it is shown in Fig.14 (a) and (b), both the ground (GS) and excited states (ES) of the orbital in the quantum dot island are expressed by black and red diagonal lines. If the magnetic field is applied into system, the spin degeneracy of both GS and ES are broken and each of states start splitting. This means that since there are two degenerate spins filled in each of the orbital states, the external magnetic field causes them to separate each other as one spin goes up and the other spin goes down and their spacing increases linearly as more magnetic field is applied.

Each of the separation between two spins splitting in orbital states follow the Zeeman energy relation as

$$\Delta E(B) = \Delta E(0) + |g\mu_B B| \tag{16}$$

where $\Delta E(B)$ is the Zeeman energy, $\Delta E(0)$ is zero field splitting energy according to the exchange interaction between the electrons in different orbital states, however this is not covered in this thesis, and g is the effective g-factor [40] [39].

Moreover, the spin states in the quantum dot are also dependent on the external magnetic field due to the broken degeneracy where the positions between two spin states are shifted and this is illustrated in Fig.15. As it is shown in Fig.15, the external magnetic field separates the conductance peaks where its orbital level is charged with either spin up or spin down. The gradient of the chemical potential for spin down states (μ_{N-1} and μ_{N+1}) is negative and spin up states (μ_N and μ_{N+2}) becomes positive as the magnetic field increases. The peak positions between two spin states follows the single-particle energy level as described above in Fig.13 as the spacing between two different orbital levels is ϵ [41].

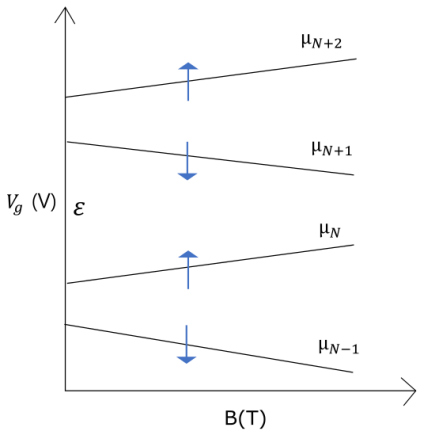

Figure 15: A change of line spacing of conductance peaks in quantum dot as the evolution of magnetic field

3 Method

3.1 Sample preparations before fabrication

In this project, the quantum dot in GaSb based SHT device is fabricated in cleanroom laboratory. The aim of fabrication is to create the quantum dot island by the Schottky contact between segments of p-type GaSb nanowires and metallic electrodes. As for the sample preparation, a silicon device chip is used for the fabrication process. The device chip is composed of degenerately n-doped silicon wafer. A 100 nm thick insulating layer of SiO_2 is thermally grown on the front side of the wafer. The conductive substrate on the backside of chip is coated by gold (Au) and this works as an electrical contact to the wafer, which in turn acts as a global back-gate when a bias is applied. The surface of the device chip contains the designed patterns of large scale contacts and the fabrication process aligns to these for nanowire deposition and contact metal electrodes and the optical microscope image of device surface is shown in Fig.16.

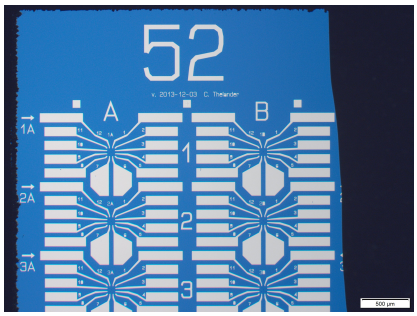

Figure 16: The optical microscope image of device surface with designed patterns of gate lines

There are a few steps to be done for cleaning the device surface before the fabrication process gets started and this will be described in appendix.

3.2 GaSb quantum dot fabrication

Figure.17 below illustrates how the fabrication process of the underlying back-gate array on the Si chip above in Fig.16 is performed in cleanroom laboratory.

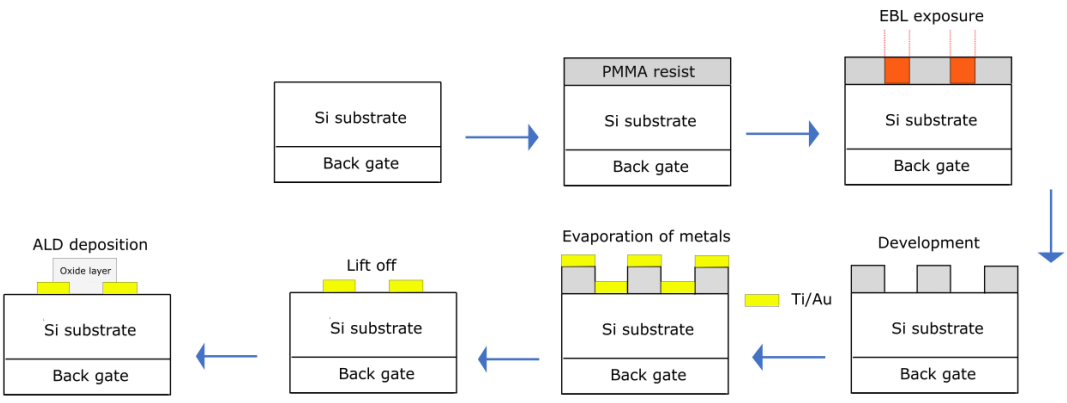

Figure 17: The fabrication process of the underlying back-gate array

A first part of the fabrication process is to determine the patterns on the device surface and it begins with coating the resist on the layer of silicon substrate. A polymethymethacrylate (PMMA) resist is covered on the surface of Si substrate by spin coating process. Electron beam lithography (EBL) is used to define the patterns on this resist surface by marking focused spots on the surface. These focused areas are removed by developing. The second part is to deposit metals on these patterned surface and this is done by using Lund Nano Lab's AVAC thermal evaporator. For these thin, underlying gates, 2 nm of titanium (Ti) and 8 nm of gold (Au) are used to coat the whole sample. After that, one needs to remove the unwanted metal that lies outside of the patterned resist. This is done by lift off process. The last part of the fabrication is to deposit hafnium oxide (HfO_2) layer on the metal surface to insulate the gate electrodes and this is performed by atomic layer deposition (ALD). There is more specific recipe of fabrication process introduced in appendix as well.

After the fabrication process is completed, the nanowires are first put on the surface and SEM images are taken to note their exact positions. The source and drain patterns are designed, exposed and metalized to form the Schottky contacted nanowire device and this is shown in Fig.18 (a). Finally, the device chip is mounted on a 14-pin electrical carrier and wire-bonded to enable electrical contact to the measurements set up.

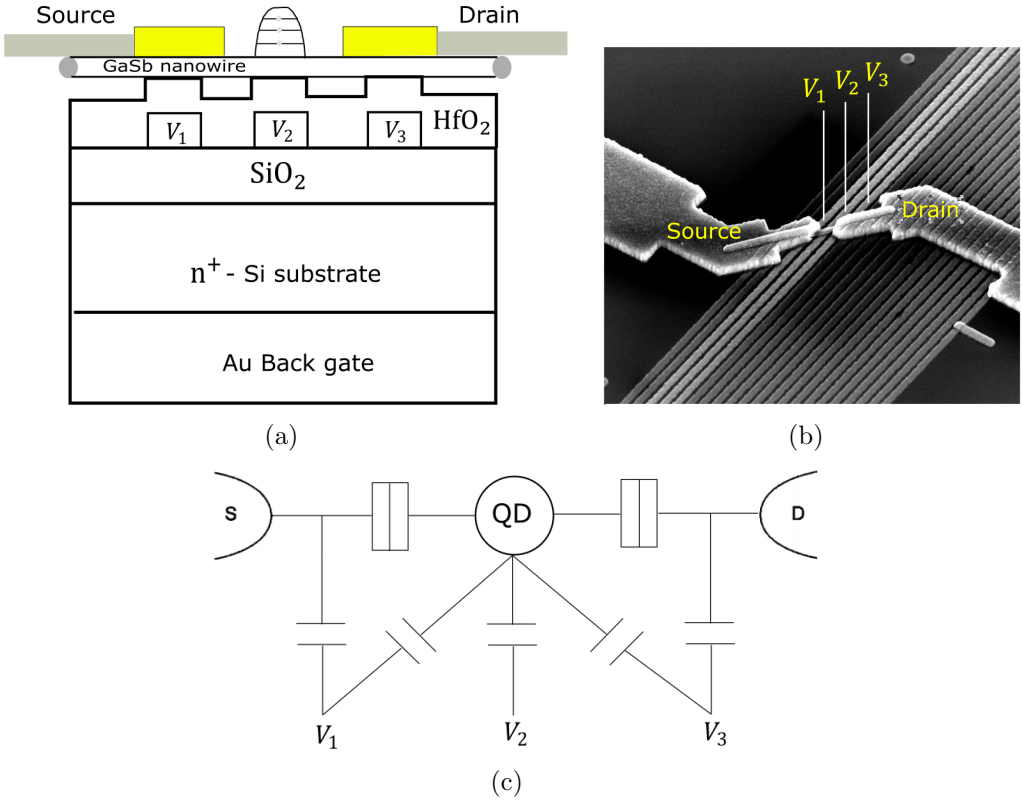

Figure 18: (a) A basic illustration of the SHT device after fabrication process is completed (b) A SEM image of the complete device (c) A schematic circuit of the SHT where the quantum dot is capacitively coupled with V_2 and cross-coupled with neighboring electrodes V_1 and V_3

A single hole transistor is produced using the Schottky barriers created when making electrical contact to the GaSb nanowire with two closely-spaced electrodes as

seen in the SEM image, Fig.18 (b). As it is shown in Fig.18 (b), there are also three underlying gates placed between the source and drain electrodes and each of them corresponds to different bottom gates (V_1, V_2 and V_3) and the quantum dot is centered above V_2. The illustration of the basic circuit diagram of SHT is shown in Fig.18 (c) where each side of quantum dot (QD) is coupled through tunnel barriers to the source (S) and drain (D) electrodes. And the additional bottom gates V_1 and V_3 are cross-coupled to the quantum dot and connected into the segment between source and left tunnel barrier (V_1) and drain and right tunnel barrier (V_3).

3.3 Low temperature measurement

As it is explained in section 2.2.1, measurements of hole transport in quantum dots should be performed at low temperature where its charging energy should be larger than thermal energy of electron ($E_c > k_B T$). In this project, an Oxford Instruments Triton 200 dry dilution refrigerator is used for the measurement. This instrument was developed by the company Oxford instruments for the research in quantum electronic technologies. The cooling system is operated by spontaneous phase separation of Helium-3 (^{3}He) and Helium-4 (^{4}He) mixtures where the temperature can be lowered to base temperature 20 mK. Figure 19 shows the interior (with the vacuum chamber, shielding and magnet removed) of the dilution refrigerator.

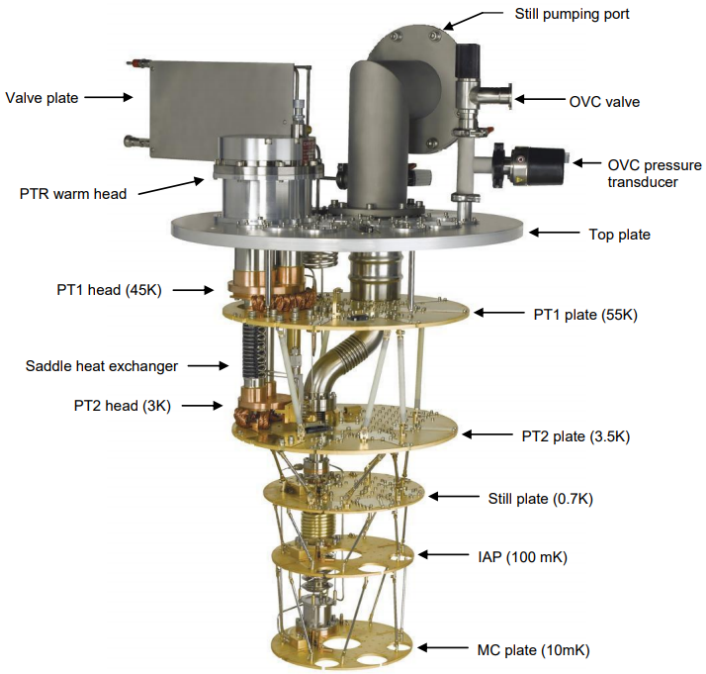

Figure 19: An interior image of Oxford instruments Triton 200 dry dilution refrigerator for the low temperature measurement (Figure adapted from [42])

The device is placed inside of sample loader and prepared for measurements. By using the systems's bottom-loading capability, the sample can be loaded while the system is around 40 k, and subsequently cooled to base within ∼8 hours. The instrument is equipped with a three axis vector magnet where its minimum magnetic field is 0 T and maximum field up to (±1, ±1, ±9) = (x, y, z) in the coordinate system. The magnetic field is applied perpendicular to the sample plane during the all of the measurements described in this thesis.

3.4 Measurement set-up

The basic measurement setup for the experiment is illustrated in Fig.20 below.

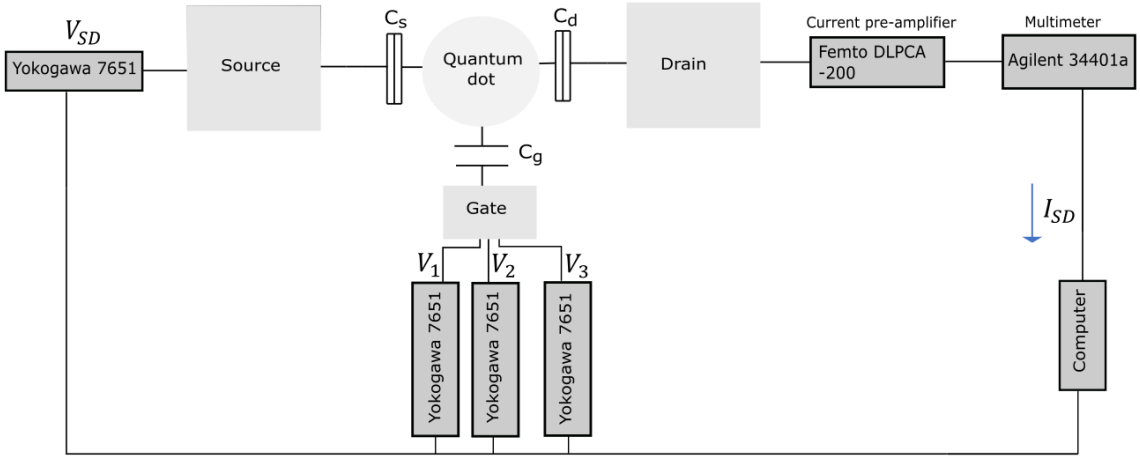

Figure 20: A schematic illustration of the low temperature measurement setup of the SHT device in the dilution refrigerator

Each of the voltage sources V_{SD}, V_1, V_2 and V_3 are connected to Yokogawa 7651 dc voltage sources. The current should be amplified by using pre-amplifier, Femto DLPCA-200 since the scale of current is in pA range. The current flowing through the device is amplified and turned into a voltage signal before being fed into an Agilnet 34401a multimeter. The whole system is operated by the computer connected with instruments via a GPIB bus and a labview program runs the measurements and saves all of the data.

4 Results and Discussions

The measurement process gets initiated with controlling the bias in each connected voltage sources by running the Labview program as follows the measurement set-up described above in Fig. 20 and the data log files are automatically saved in the computer.

A first task is to characterize the device and begin by studying the impact of different gates then investigate to find ranges in which the device is operated in a clean single or multi-quantum dot regime. The formation of double quantum dot is caused either by the valence-band roughness and the formation of multiple conductive puddles for low occupancy states or by additional quantum dots induced by V_1 and V_3 [9]. The starting point is to investigate double quantum dot formation in the low occupancy states by the valence-band roughness while for high occupancies, the system acts as expected from a single quantum dot (SQD) with the formation of Coulomb diamonds as described above in Fig.11 (b). This can be done by building a charge stability diagram by sweeping V_{SD} as a function of V_2 while applying 0 V bias to gates V_1 and V_3 and then observe the Coulomb diamond patterns. The assumption is that one should observe clear shaped Coulomb diamonds if the SHT is a single quantum dot island but its diamond patterns will no longer be clearly formed when the island starts to deform and a multi-dot system is formed. Next, the multi quantum dots formation by the additional gates are investigated and this can be studied by building a charge stability diagram by sweeping gates V_1 and V_3 as a function of V_2 and observe how the addition of hole states are different in between single and multi-quantum dot states.

First, an arbitrary starting point is chosen where V_1 and V_3 remain grounded and the charge stability diagram as a function of V_2 is recorded. The voltage sources are selected to be -10 mV $\leq V_{SD} \leq$ 10 mV with the arbitrary range of high occupancy regime in negative gate voltages, -2 V $\leq V_2 \leq$ -1.7 V and keeping $V_1 = V_3 = 0$ then its charge stability diagram is shown in Fig. 21. The limit of the voltage applied into bottom gates and source-drain bias is ±3 V and ±10 mV respectively to avoid damage of the devices.

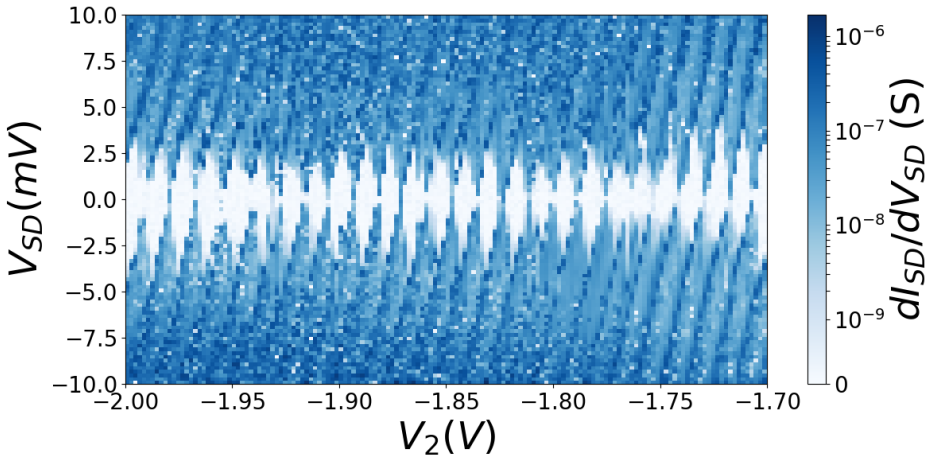

Figure 21: A charge stability diagram of the SHT while sweeping V_{SD} as a function of V_2 in the range -2.0 V $\leq V_2 \leq$ -1.7 V in high occupancy quantum dot regime. The diagram is plotted in linear with logarithmic scale while this holds for other plots

The clear formation of Coulomb diamonds can be seen in Fig. 21 over the measured range of V_2. This indicates the clear Coulomb blockade effect of the SHT whether the hole transport through the p-type quantum dot is allowed or blocked depending on the value of V_2. And this is not expected to observe the double quantum dot formation since the clear shape of diamond patterns are not broken in this range. Therefore, one starts applying more positive range of V_2 then investigate its effect and this is illustrated in Fig. 22.

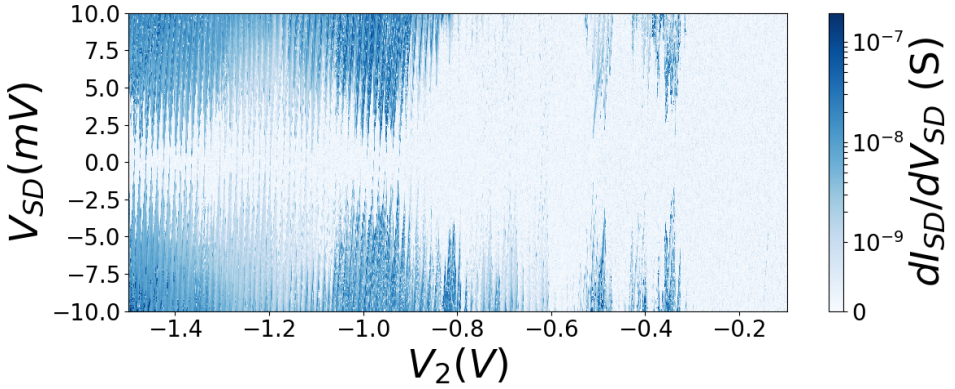

Figure 22: A charge stability diagram of the SHT while sweeping V_{SD} as a function of V_2 in the range -1.5 V $\leq V_2 \leq$ -0.1 V in the low occupancy quantum dot regime

As it is shown in Fig. 22, the shape of Coulomb diamonds becomes broken as more positive range of V_2 is applied and this patterns of closed diamonds is no longer observed when V_2 exceeds -1.1 V where the SHT begins to have more than one quantum dot due to puddles formed at the rough valence band edge. This shows that the single quantum dot island starts to be deformed and turns into a multi-dot system where the similar features are observed from the previous research in p-type silicon quantum dot [9]. In other words, the behaviour of single or multi-quantum dot system is highly dependent on the occupancy of states. At a higher occupancy of states with small positive V_2, the first few holes entering into the quantum dot are further away from the roughness of the valence band edge and the system thus acts as a clean quantum dot in this regime. However, if there is more positive V_2 applied and the system goes into a lower occupancy of states, the holes entering into the quantum dot are energetically close to the band edge at the potential well and becomes vulnerable to the roughness which turns into multi-quantum dot system and this is illustrated in Fig. 23 [9].

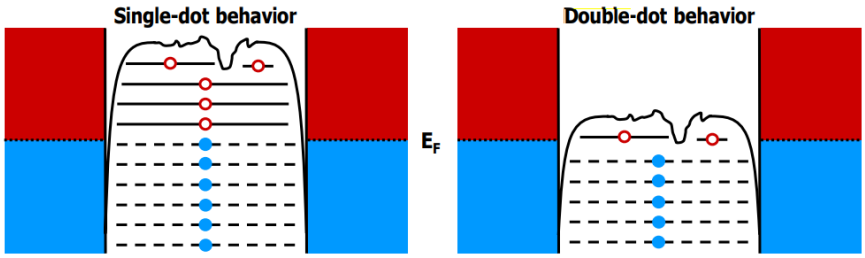

Figure 23: A diagram of a single quantum dot island in the SHT and its effect in bottom of the potential well while applying positive bias in V_2 and turning into a double quantum dot (Figure adapted from [9])

A next task is to study the effect of a voltage applied into the outer gate stripes V_1 and V_3. This is done by stepping gate V_1 and V_3 as a function of V_2 as shown in Fig. 24. The charge stability diagrams as a function of the middle gate, V_2 at different ranges of barrier gate, V_1 are seen in Fig. 24 (a) and (b). Similarly, different ranges of barrier gate, V_1, as a function of the middle gate, V_2 are shown in Fig. 24 (c) and (d).

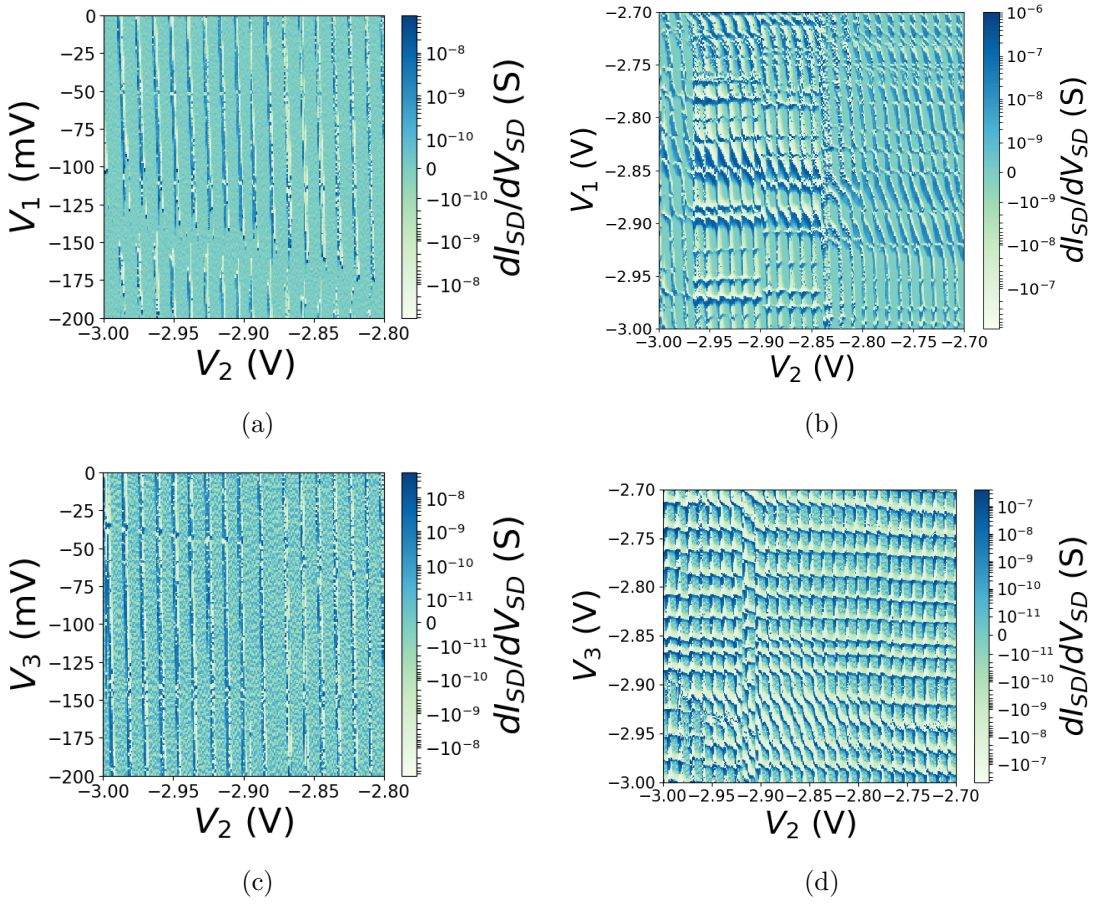

Figure 24: Charge stability diagrams of combinations of two bottom gates, V_1 and V_2 in two different range for (a) and (b), V_2 and V_3 for (c) and (d) with a fixed set of third gate voltage to be 0 V in (a) and (c), -3 V in (b) and (d)

Figure 24 (a) and (b) describes the multi-dot formation by the effect of V_1 as well as (c) and (d) is by V_3 gate. At more positive range of V_1 and V_3 as shown in Fig. 24 (a) and (c), the charge stability diagram shows the patterns of vertical line crossing horizontal axis while applying V_2. Each of the vertical lines corresponds to the number of hole states and once the next hole states are added into the SHT, another line is created and this is illustrated in Fig. 25 (a) which describes the simple model for the hole addition states in single quantum dot. These shows that the addition of hole states are highly dependent on gate V_2 which is directly capacitively coupled into the quantum dot. On the other hand, the additional gates, V_1 and V_3 have less contributions to these hole addition states in this positive range. If the SHT contains a pure single quantum dot system, one might expect to detect strict vertical lines as the number of hole states increase. However, V_1 and V_3 are also cross-coupled into the quantum dot in this case and this causes the gradient shift of vertical lines as it is observed in Fig. 24 (a) and (c).

As more negative values of V_1 or V_3 are applied, the horizontal features start to emerge in addition to the vertical lines and forming honeycomb lattice patterns as shown in Fig. 24 (b) and (d). In general, these patterns are usually caused by two capacitively coupled quantum dots and the change of electrostatic energy of one quantum dot by addition of a hole in the other quantum dot and the cross coupling of each quantum dot by other gates [31]. The simple model of the hole addition states for the double quantum dot is illustrated in Fig. 25 (b) with the formation of coordinates system where the hole additions are dependent on two outer gates V_1 and V_2. The N is the hole state in the middle (right) and M is the outer, for the quantum dot formed by V_1 left.

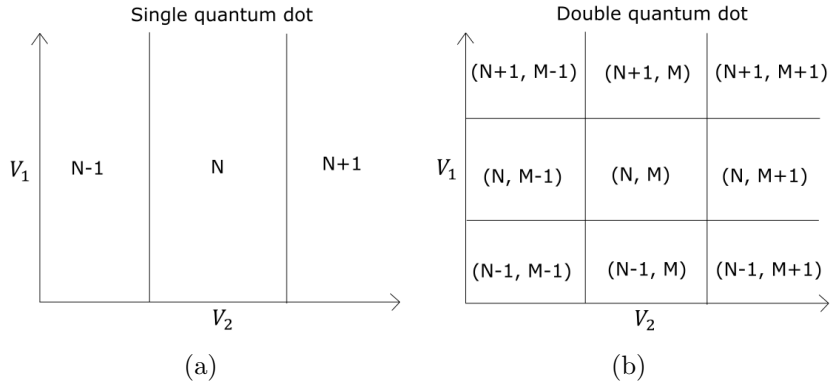

Figure 25: A simple model of the charge stability diagram for single (a) and double quantum dot

The action of gate on the nanowire is distinctly restricted and its impact is limited to the nanowire segment which is directly coupled into the each gate stripe. Therefore, the gaps between each of the gates in the array always works as a tunnel barriers. In addition with the Schottky-contacts, this leads to the formation of a hybrid system between a serial and parallel double quantum dot [43]. In actual case, the additional islands created by higher negative bias applying in V_1 and V_3 causes the shift of tunnel barriers coupled into source and drain electrode. This is because the middle quantum dot which is capcitively coupled into V_2 should be always directly tunnel coupled into source and drain electrode and the basic circuit of double quantum system formed by gates V_1 and V_2 is illustrated in Fig. 26.

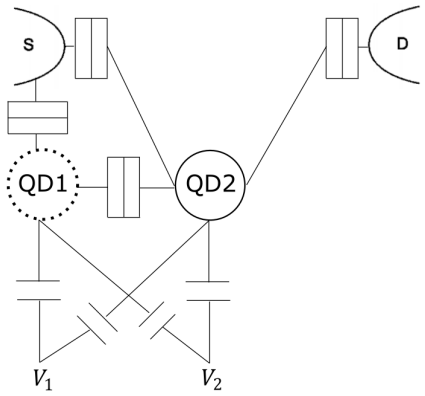

Figure 26: A double quantum dot circuit formed by middle quantum dot coupled into V_2 and left quantum dot created by V_1.

As it is shown in Fig. 26, each of the gates, V_1 and V_2 are cross coupled into the other quantum dot (V_1 with QD2 and V_2 with QD1) and the middle quantum dot, QD2 are directly tunnel coupled into both source and drain electrodes. The middle dot, QD2 is also tunnel coupled with left quantum dot QD1 which is created by V_1 and the electrical conductance is affected by the exchange of hole transport between two coupled quantum dots. The QD1 should only be tunnel coupled with source electrode since the bottom gate stripe, V_1 has direct contact with this electrode as shown for the SEM image in Fig.18 (b).

According to the preliminary results in Fig. 22 and Fig. 24, it was obtained in which range of all three bottom gates V_1, V_2 and V_3 should be applied into circuit in order to keep single quantum dot behaviour. In the single quantum dot case, the regions of constant charge are almost exclusively (neglecting a weak cross coupling) defined by V_2. In contrast, if the additional quantum dots are formed, the regions of constant charge now depend on the two different quantum dots and are thus also dependent on the voltage applied into V_1 or V_3.

It was previously observed that the roughness of the valence band leads to the formation of small quantum dot 'puddles' for low occupancy states (higher positive V_2) and the Coulomb diamond is no longer detected [9]. If the dimensions of the quantum dot becomes smaller, there is less space for these puddles to be occupied and hence cleaner single quantum dot behaviour with formation of Coulomb diamonds is expected. In addition, the smaller quantum dot size leads to an increased energy spacing between orbital levels due to quantum confinement effect and this might increase the resolution between ground and excited states of quantum dot, which in turn leads to the clear formation of Coulomb diamonds as well. Reducing the size of the quantum dot can be done by controlling and applying more positive voltage to V_1, V_3 and backgate, V_{BG}. This will force the nanowire segments around V_2 to be non conductive and will thus ideally limit the conductive island forming above V_2 to a smaller size.

Figure 27 shows two charge stability diagrams measured at different values of V_1, V_3 and V_{BG}. The values are fixed to be $V_1 = V_3 = 1$ V and $V_{BG} = 3$ V for (a) and $V_1 = V_3 = 1.5$ V and $V_{BG} = 4$ V for (b).

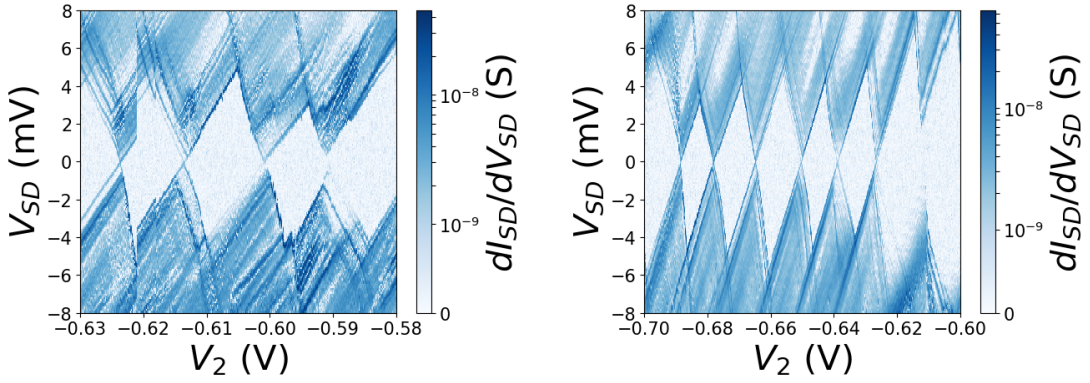

Figure 27: Charge stability diagrams with different ranges of bottom gates $V_1 = V_3 = 1$ V and $V_{BG} = 3$ V for (a) and $V_1 = V_3 = 1.5$ V and $V_{BG} = 4$ V for (b)

Comparing these charge stability diagrams with previous case of Fig. 22, one could start observing clear shaped of Coulomb diamonds at low occupancy states with higher positive range of V_2. This shows that quantum dot becomes smaller and thus the roughness of the valence band is less impactful even at more positive V_2 values. The setting in Fig. 27 (b) creates much clearer shape of Coulomb diamond than (a) as the sides of diamond rhombus are more flattend and these conditions are set for future measurements.

In Fig. 27 (b), the lowest consecutive 6 hole occupancies for which clean single quantum dot behaviour is observed and identified. The magneto-transport properties are investigated in this range by applying the magnetic field always perpendicular to the samples and nanowires. Initially, a series of 6 consecutive coulomb peaks with a clearly resolved charge stability diagram in Fig. 27 is found where this range should be studied for device properties by using magneto-spectroscopy techniques. As for the first step, one investigates the shift of Coulomb peaks as a function of magnetic field applied perpendicular to the device plane. For B=0 T, the Coulomb peaks are observed in the range of -0.7 V $\leq V_2 \leq$ -0.62 V at a fixed bias of $V_{SD} = 0.5$ mV in Fig. 28 (a). The Fig. 28 (b) shows the evolution of peaks as a function of the magnetic field from 0 to 6 T, where each of the vertical lines in the differential conductance plot corresponds to one of the Coulomb peaks in (a).

The spin filling states in each conductance peaks are expected to follow the two-fold degeneracy model of single particle energy level states as described above in Fig. 13 where the order of alternating spin is filled in the orbital level. According to Fig. 15 which describes the standard model for the behaviour of conductance peaks in each spin states by applying the magnetic field, the peak positions are shifted as the magnetic field increases since two opposite spins occupied in different states are separated as a function of magnetic field [41]. However, the conductance peaks of spin states in Fig. 28 does not match with any of these models since it is difficult to determine the change of line spacing between each peaks even if the magnetic field increases. The source-drain bias, V_{SD} was set to be 0.5 mV and the resolution between peak separations should be enhanced by applying smaller bias voltage, however this is not covered in this project. This provides a further implications about the possible range of g-factor taking by separation of two opposite spins in orbital state later. Equation 16 gives the linear relation of energy differences between spin states and the magnetic field. Due to the width of the peaks caused by the source-drain bias applied in Fig. 28 (a), the maximum g-factor that could be masked in the corresponding energy range is calculated to be 1.01.

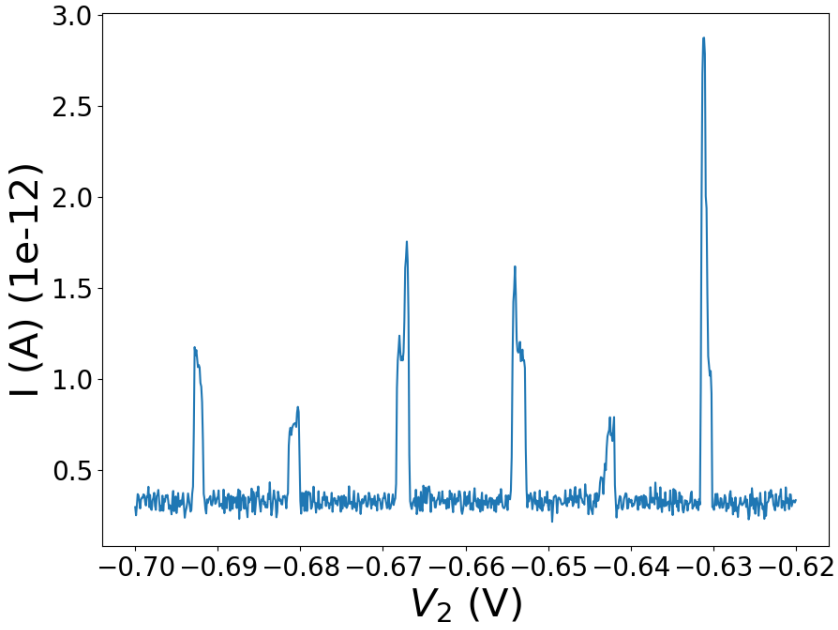

(a)

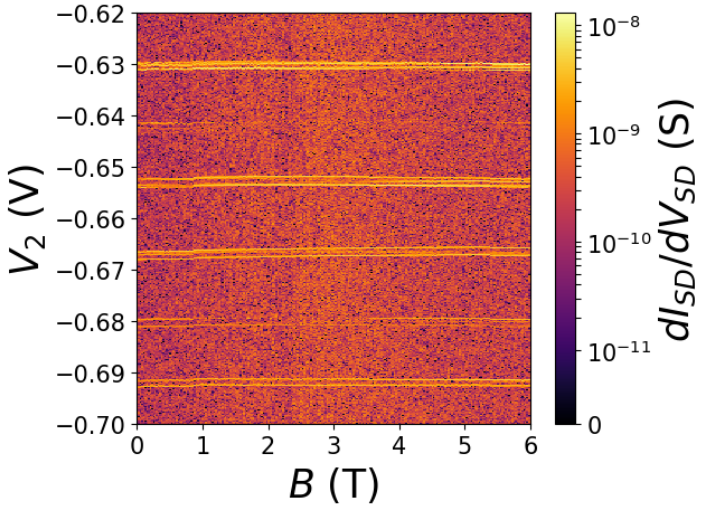

(b)

Figure 28: (a) A Coulomb oscillation of conductance peaks at the negative range of V_2 with fixed set of $V_{SD} = 0.5$ mV (b) A linear response of conductance peaks as a function of applying magnetic field, B

Figure 28 indicates the Zeeman effect of spin states in conductance peaks. Now, the Zeeman effect of the orbital excited states is investigated and the effective g-factor is extracted by Zeeman splitting of spin-degenerate states as a function of the magnetic field. The line spacing between two splitting peaks as a function of magnetic field, B is plotted then the g-factor can be measured by taking the gradient of the plots and this follows Eq. 16 as described above. As for the first step, one should decide which orbital excited states are selected in the Coulomb diamond. This can be done by taking the vertical linecuts on the edge of hole occupancy states in the Coulomb diamond. In this case, there are 6 different linecuts for V_2 chosen in charge stability diagram which are A : -0.6925 V, B : -0.6911 V, C : -0.679 V, D : -0.668 V, E : -0.6450 V and F : -0.631 V and these are illustrated in Fig. 29.

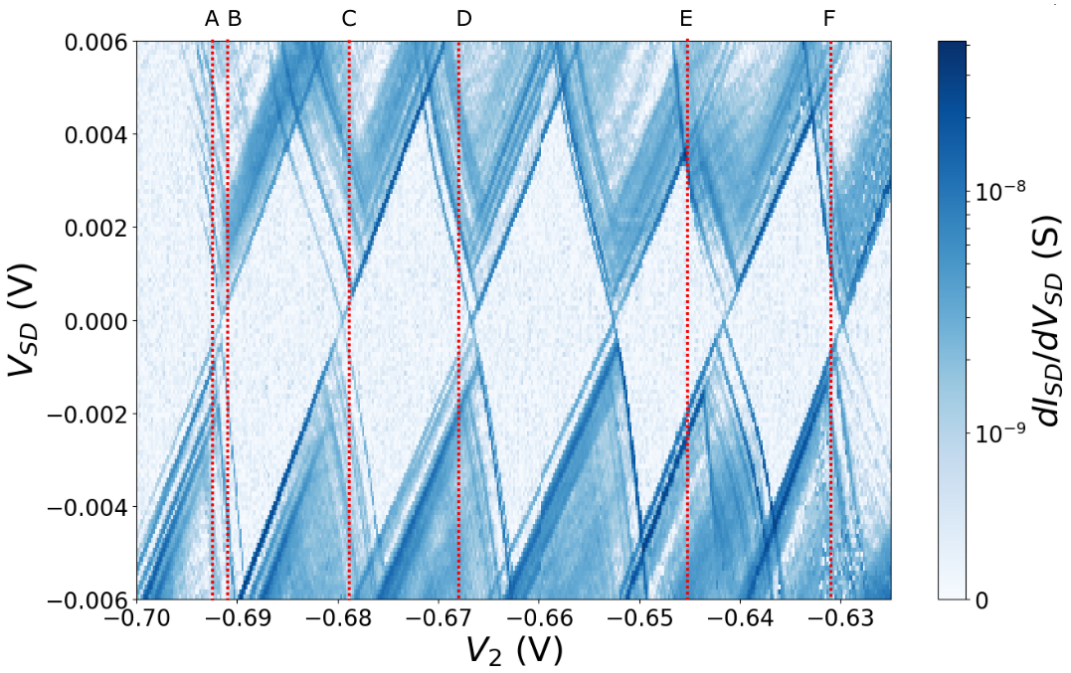

Figure 29: A charge stability diagram with different vertical cutlines marked in V_2

Figure 30 (a), (c), (e) and (g) show the single Zeeman splitting of spin states in the Coulomb diamond which corresponds to linecut of D, F, B and C from the top of Fig. 29 and these match with each of the scattered plots of line spacing between two splitting peaks as magnetic field increases and its best fit lines, Fig. 30 (b), (d), (f) and (h). A negative bias of V_{SD} is applied in linecut B and rest of them are applied by positive bias. The effective g-factor, $|g|$ is calculated by using Eq. 16 and this yields $|g^*| = 3.8 \pm 0.1$, $|g^*| = 2.4 \pm 0.1$, $|g^*| = 4.6 \pm 0.3$ and $|g^*| = 2.3 \pm 0.1$. Each of the linear fits error were found to be $\pm$ 0.09, $\pm$ 0.04, $\pm$ 0.3, $\pm$ 0.02. However, this is an uncertainty of the best fit line and does not provide any information about error of g-factor itself. As for the main uncertainty, one should take into account the finite resolution of the data with peak identification, selection of proper data-points with the step size and the addition of hole states by finite temperature effect in Fermi Dirac distribution. Therefore, the selection of reasonable uncertainty scales of g-factor should be around one significant digit, $0.1\sim$ and this holds for other fit lines. The zero field energy, $\Delta E(0)$ in Eq. 16 assumes that the energy is zero when the magnetic field, B=0 T since there is no splitting at that point. However, most of the linear fits does not follow this assumption except for the case Fig. 30 (d) because these fits are not enforced to be adjusted into Eq. 16. This can be fixed by decreasing the step size of scattered plots and including only the spots which belongs to the edge of best fit lines. However, this might cause the reducing accuracy of effective g-factor.

Moreover, one can identify Zeeman effect of single and triplet spin states. Figure 31 shows how the spin filling states in both ground and excited states in the orbital determines the splitting for singlet and triplet spin states of the quantum dot. As it is shown in Fig. 31 (a), the ground state of the two-hole quantum dot has a spin singlet state where total spin number is S = 0 by filling two opposite spins in the single particle energy levels at B=0. The first excited states with red dashed line has the spin triplet states where total spin number is S = 1 where the spin quantum

number, $m_s = 0$ with wave function, $|T_0\rangle = \frac{1}{\sqrt{2}}(|\uparrow\downarrow\rangle + |\downarrow\uparrow\rangle)$. The other wave functions for spin up state is $m_s = 1$ with $|T_+\rangle = |\uparrow\uparrow\rangle$ and spin down state is m_s = -1 with $|T_-\rangle = |\downarrow\downarrow\rangle$ [31]. Figure 31 (b) shows how the singlet state with single spin down in ground state and triplet states with two paired spins in excited states behave when the magnetic field is applied. The down-spin in singlet state goes down in energy as the magnetic field increases since the half integer spin can not split. However this depends on the sign of the g-factor since it is undefined which orientation of spin is filled on the state and this is reason why one should take the absolute value of g-factor. For example, the line spacing between two conductance peaks in spin states is calculated by taking the differences between up-spin and down-spin states. And, it was assumed that splitting of upper peaks corresponds to up-spin and down-spin for the bottom peaks in each panels (a), (c), (e) and (g) which means that spin orientations was not clearly defined in this case.

The two paired spins in triplet states split into T_+ for up-spin and T_- for down-spin as magnetic field increases and the spacing between singlet and triplet states is expected to be single particle energy level differences, ϵ in different orbital states of the exchange energy. It is indicated that the charge transport in quantum dot is dominated by only two excited triplet states T_+ and T_-. And, the similar behaviour was observed from the previous research in InAs quantum dot where the charge transport on the system is contributed by two triplet states T_0 and T_+ due to the fast relaxation of spin and weak coupling between quantum dot and lead electrodes [15]. Figure 30 (e) shows the closest behaviour with this model even if the excited states (ES) splits into either more or not than two lines. Figure 30 (c) also shows the similar trend of splitting as (e), however this singlet and triplet splitting model can not be applied in this case, since the ground state (GS) splits rather than excited states. The panel (a) in linecut D did not show any distinct effect of these singlet and triplet state properties except for detection of one splitting orbital state. As for the panel (g) in linecut C, the bottom splitting peaks of orbital states become constant around at B = 3.5 T and does not split anymore. This might be because the bottom peak undergoes an avoided level crossing with a higher excited state peak which is not detected in this panel. The avoided level crossing is the result of the spin-orbit interaction between two different states since these eigenstates do not interfere with each other [10] [44]. This shows that the values of effective g-factors are highly dependent on hole occupancy states and also affected by strength of spin-orbit interaction on the state.

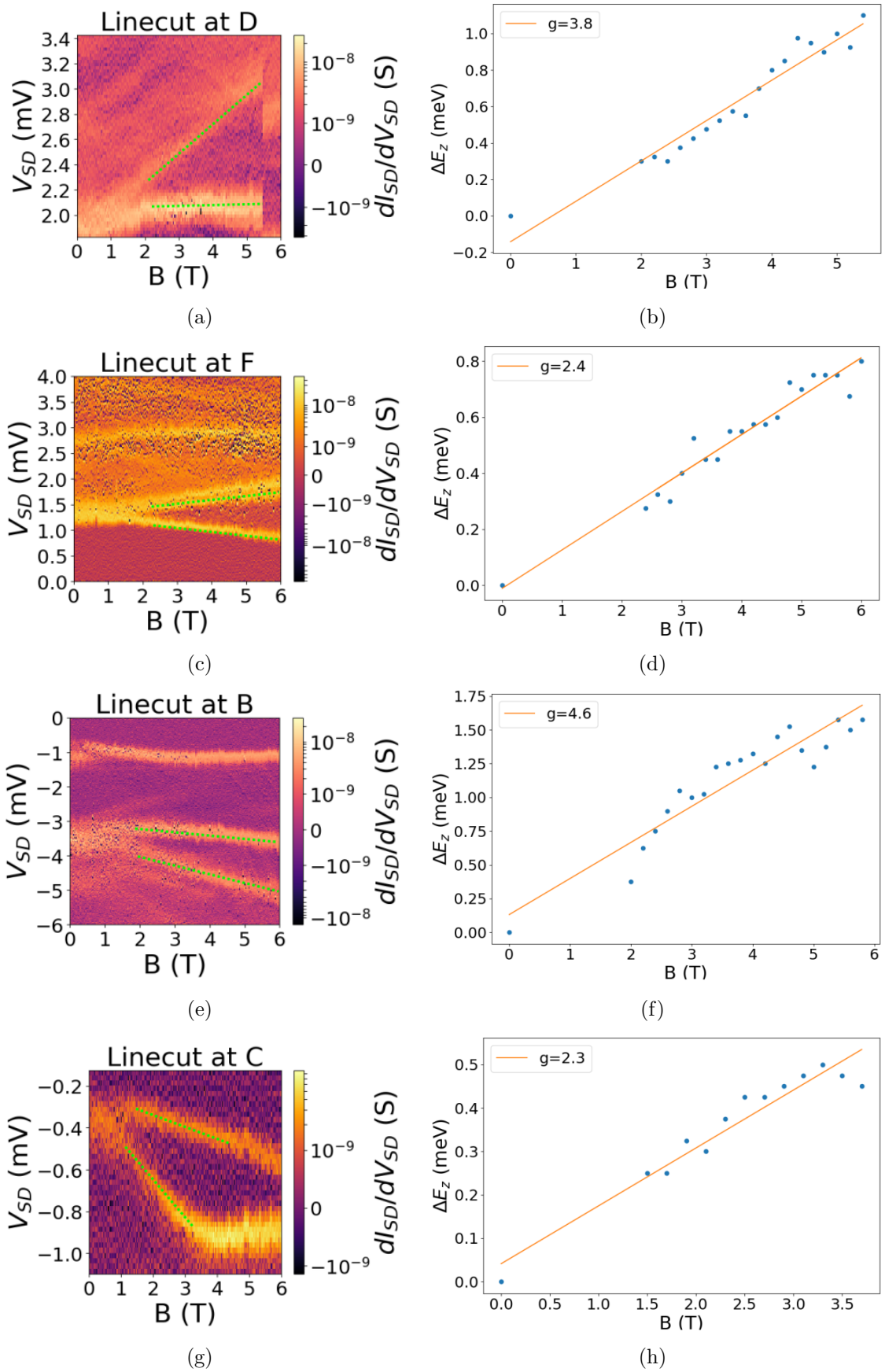

Figure 30: A single Zeeman splitting of spin states in different hole occupancy states with g-factor. (a),(c),(e),(g) are raw data at linecut D, F, B, C and (b),(d),(f),(h) are the extracted energy splittings

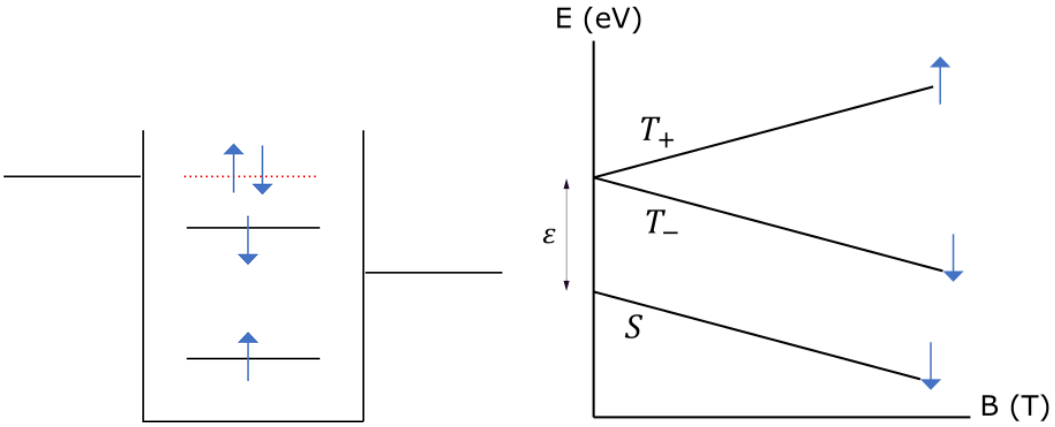

Figure 31: (a) A spin filling states in ground and excited states of the orbital in quantum dot. (b) A simple model of zeeman splitting for singlet and triplet spin states of quantum dot where the charge transport is dominated by two triplet states T_+ and T_-

Figure 32 (a), (b) shows the behaviour of multiple splittings of spin states of the quantum dot in linecuts of E and A. Figure 32 (a) consists of two spin-degenerate levels splittings in the ground state where the each of g-factor is $|g^*| = 1.8 \pm 0.1$ (bottom) and 2.2 ± 0.1 (top) as shown in Figure 32 (c) and (e). However, this behaviour can not be explained by the singlet and triplet states model described above since there are three different splittings observed in this case. It might be because the linecut E is close to the tip of Coulomb diamond which allows the three different charge states at the same time and makes the interpretation complicated. In Fig. 32 (d), the two spin degenerate levels at B=0 in both ground and excited states have Zeeman splitting with an applied magnetic field. The g-factors for each of the GS and ES states are equal to be $|g^*| = 1.3 \pm 0.1$ as shown in Fig. 32 (d) and (f). It is observed that the two splitting peaks are not interfered each other and undergoes an avoided level crossing due to the spin-orbit interaction between two states (bottom peak of the ground state and top peak of the excited state). The value of gap energy between two peaks is ΔE approximately 225 μeV by taking the difference between two splitting peaks at the point where it starts to be avoided which is around at B=3.1 T and this gives the spin orbit interaction energy as $\Delta E/2$, which is $E_{SO} = 113$ μeV.

The effective g-factors by splitting of spins in orbital states were extracted as a function of the applied magnetic field in different hole occupancy states of the Coulomb diamond as shown in Fig. 30 and Fig. 32. The preliminary results show that g-factors are affected by the spin-orbit interactions on the states. Linecut A shows the distinct effect of spin-orbit interactions has the smallest value of g-factor than other panels. One can assume that this might be because spin-orbit interaction leads to an underestimate of the g-factor. There should be more cases similar to linectut A with clearly resolved avoided level crossings investigated. This can be done by improving the resolution of each panel and detecting avoided level crossing peaks or selecting better linecuts of hole states in the Coulomb diamond as it was done in Fig. 29.

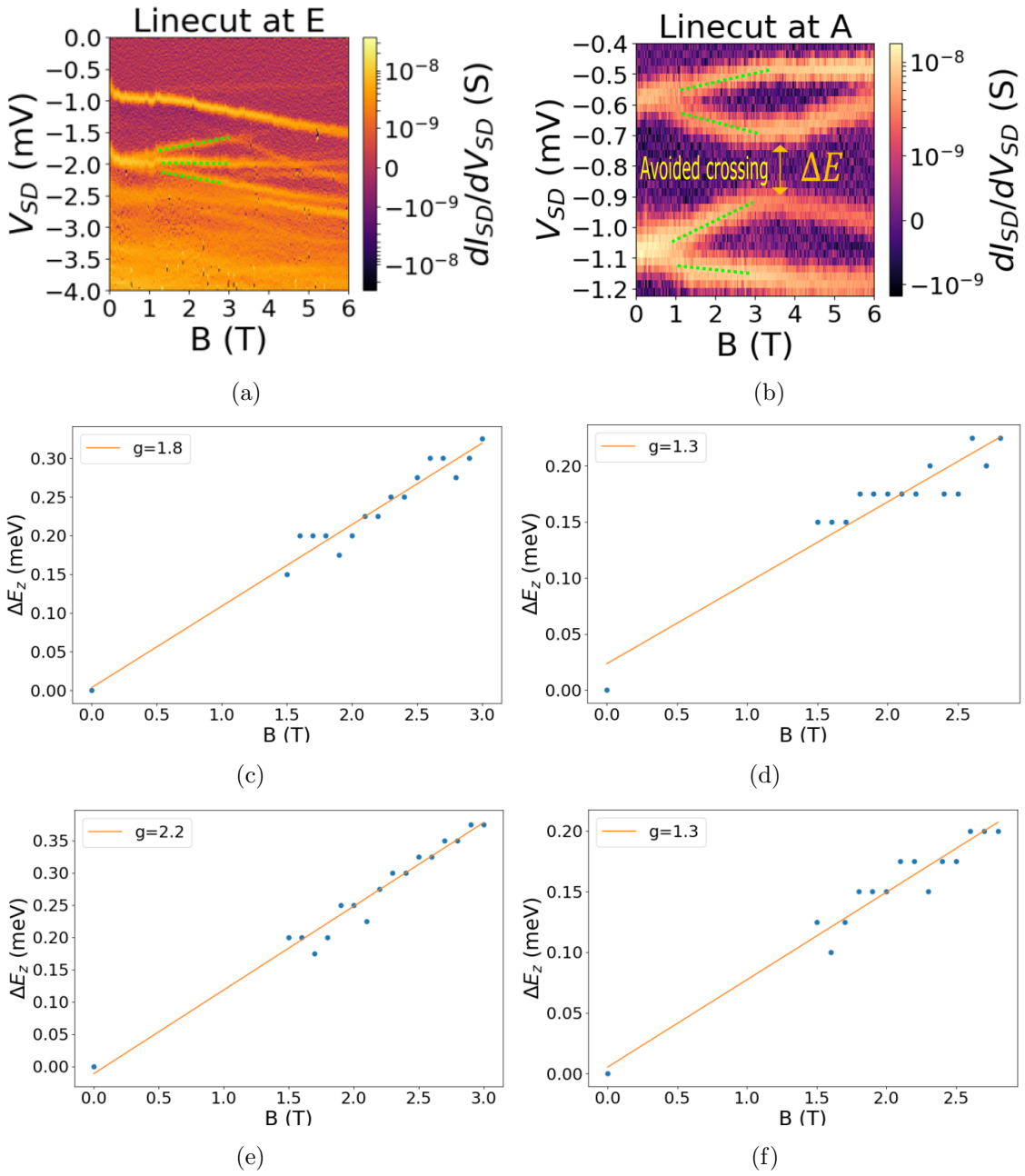

Figure 32: A multiple Zeeman splitting of spin states in different hole occupancy states with g-factors. (a),(b) are raw data at linecut E, A and (c),(d),(e),(f) are the extracted energy splittings

5 Conclusions and Outlook

In this project, the hole transport through quantum dots in GaSb nanowires was investigated. The SHT of p-type GaSb quantum dot consists of three different bottom gates where the middle gate strip is directly- and two outer gates are cross- coupled into the quantum dot. First, the effect of each gate on the device was characterized. It was observed that SHTs are inclined to have single quantum dot behaviour at higher values of negative of V_2 (higher occupancy states) and higher positive ranges of V_1 and V_3 and this was determined by the shape of the Coulomb diamond patterns. The effect of smaller dimension of quantum dot was also investigated by tuning the biases of each of the bottom gates and the backgate, V_{BG}. The clear shape of Coulomb diamonds was detected at lower occupancy states as the quantum dot size starts to decrease. This indicates the importance of the valence-band roughness which prevents the formation of clean single QDs for larger quantum dots at low occupancies. The relation between spin states of conductance peaks and external magnetic field was also investigated but it was not clearly identified to find their dependence except for the assumptions of minimum expected value of g-factors. Finally, the effective g-factor by splitting of spin degenerate states as a function of magnetic field was investigated at different hole occupancy states in Coulomb diamond. The values of g-factor varied from $1.3 \sim 4.6$ and they are highly altered by avoided level crossing between two splitting Zeeman states and this causes the underestimate of extracted g-factors by using the linear fit method.

The results obtained in this project agree with the outcomes from previous research with respect to hole transport behaviour in different occupancy states and the formation of either single or double quantum dots [9]. For example, the collapse of single quantum dot behaviour into double quantum dot at lower occupancy of hole states due to the roughness of the edges in valence band follows the research from hole transport in Si nanowire quantum dots [9]. This shows that the GaSb quantum dot follows the general behaviour for the hole transport compared with other p-type materials.

The magneto-spectroscopic behaviour of the GaSb quantum dot is clearly distinguished with other quantum dot materials. First of all, the Zeeman effect of spin states in conductance peaks are clearly indicated in n-type InAs nanowire [41]. In this case, the alternating spin filling in two different states are separated as a function of magnetic field. On the other hand, in this project, these behaviours are not clearly detected and one expects to observe clearer behaviour by controlling the resolution to step size given by electron temperature. Second, the extracted effective g-factor and the spin-orbit interaction energy of GaSb quantum dot are different with other quantum dot materials as well. According to the previous research, there are different values of spin-orbit interaction energy for other semiconductor materials obtained as $E_{so} = 0.044$ eV (Si), $E_{so} = 0.34$ eV (GaAs), $E_{so} = 0.29$ eV (Ge), $E_{so} = 75$ μeV (GaSb/InAsSb core shell), $E_{so} = 0.25 \sim 1$ meV (InSb), $E_{so} = 15 \sim 135$ μeV (InAs) and $E_{so} = 90 \sim 600$ μeV (Ge/Si core shell nanowires) [45] [10] [46]. The spin-orbit interaction energy of GaSb quantum dot obtained in this project is $E_{so} = 113$ μeV. This shows that the value of E_{so} in the GaSb quantum dot is much smaller than Ge and GaAs, however it is comparable with other group III-V materials in a range of $\sim$100 μeV such as InAs or GaSb/InAsSb. This spin-orbit interaction is

one of the most important factors to be considered in quantum computation, since the relaxation and decoherence of spin states in qubit is determined by spin-orbit interaction. This is because the charge fluctuations induced by the coupling between spin and the charge in the orbital is dependent on this spin-orbit interactions [15]. And, InAs is already proven as prominent material to control the motion of the electron/hole by the strong spin-orbit interactions which indicates that GaSb can be another candidate material to be used in quantum computation technology as for the future research [47]. The effective g-factor in GaSb lies in the range of other p-type material such as GaSb/InAsSb core shell where the obtained g-factors are around $1.17 \sim 4.7$ [10].

The results indicate the hole transport behaviour of SHT devices in terms of degree of gate control, occupancy of hole states, spin-orbit interaction and the Zeeman effect. The high spin-orbit interaction energy proves that the GaSb quantum dot is potentially to be applied into quantum computation research since the strong spin-orbit coupling allows the more precise control of orientation and motion of electron/hole spins in quantum dot [48]. Therefore, one can start fabricating serial double quantum dots as for the qubit prototypes in the outlook. The fabrication process should be performed similarly as described above in section 3.2 as the quantum dot is created on the gate by the Schottky contact between nanowires and metal electrodes. The starting point is to create the multi-quantum dot system by using five different bottom gate lines where the two outer gates V_1 and V_5 are connected with source-drain electrodes and the gates V_2 and V_4 works as the bottom gates for two serial coupled left and right quantum dots and the tunnel barriers between these two quantum dots are controlled by gate V_3 to create the double quantum dot system [13]. However, as it is mentioned above in the result section, the nanowire segment connected into gate stripe is affected by the gate action and its gaps between the gates works as tunnel barriers. These causes the formation of triple quantum dot (TQD) states in series induced by three bottom gates V_2, V_3 and V_4 and preventing serial coupled double quantum dot (DQD) formation. In order to solve this problem, the current device architecture should be able to control these gaps between the gates on the nanowire segments. This can be achieved by combining both bottom and top/side gates or stacking bottom gate arrays in such a manner that entire positions of nanowire segments are controllable [13].

A Appendix A

A.1 Sample preparations

- Device soaks in a beaker of acetone and placed in ultrasonic (US) bath cleaner and run for 3 minutes
- Repeat the above process after switching the sample from a beaker of acetone (Ac) into a beaker of isopropanol (IPA)
- Device surface is sprayed using nitrogen N_2 gun to evaporate remaining isopropanol from the surface

A.2 Sample fabrication

- Use the Labview software and auto-electrode to design the patterns of bottom gates with 50 nm lines and 50 nm distance with 0.9 dose factor
- Ashing the sample by using oxygen (O_2) plasma asher with a pressure of 5 mbar
- Pre-bake the device for 1 minute at 150°C
- Spin coat the ARP 6200.04, 6000rpm resist on the Si substrate surface for 1 minute and bake it again for 1 minute at 150°C
- Use EBL-Raith of 30 kV, 10 μm, 0.015 nA with dose of 90 $\mu C/cm^2$ and define the patterns on the surface by focused marks
- Develop the patterned surface with amylacetate and IPA for 1 min and 15 seconds respectively
- Ashing the sample by using the plasma asher with exposing 5 mbar O_2 for 12 seconds
- Evaporate 2 nm of Ti and 8 nm of Au on the surface by using Evaporator AVAC
- Lift off the unwanted metal on the outside of patterned resist by using solvent remover-1165 then heated up to 90°C for 10 minutes. Place the sample in ultrasonic batch cleaner and run for 1 minute. Use the remover-1165 again and heated up 90 °C for 5 minutes
- Ash the sample by plasma asher with exposing 5 mbar O_2 for 30 seconds
- Deposit HfO_2 layer on the surface of device by ALD deposition process
- Place the sample on ultrasonic bath cleaner and run for 1 minute. The sample soaks in a beaker of IPA and the surface is sprayed by N_2 gun
- Ashing the sample by plasma asher with exposing 5 mbar O_2 for 30 seconds
- Deposit the intermediate doped nanowires, GaAs/GaSb:Zn on the sample surface and check the position with SEM
- Use the Labview and Raith 150 software to design the patterns of quantum dot with 3 different bottom gates and soruce-drain contacts

- Spin coat the PMMA 950A5, 5000rpm resist for 1 minutes and bake it for 3 minutes at 180°C
- Use the EBL raith with 30 kV, 10 μm to complete the alignment and making 3 points of focused spots on the sample
- Develop the sample with 1:3 ratio of Methy isobutyl ketone (MIBK) and IPA for 45 seconds. Repeat it with IPA for 20 seconds
- Ashing the sample with plasma asher by 5 mbar O_2 for 20 seconds
- Oxide etching the sample with 1:10 ratio of Hydrogen chloride (HCl) and IPA for 35 seconds. Rinse the sample in IPA for 15 seconds. Spray the sample surface by N_2
- Deposit 25 nm of nickel (Ni) and 75 nm of gold (Au) by using Evaporator AVAC
- Lift off the sample with acetone heated up to 60°C for 15 minutes with pipette blow. Repeat it again with heated acetone for 5 minutes with pipette blow. Complete the Lift off process with IPA and N_2.
- Ash the sample by plasma asher with exposing 5 mbar O_2 for 30 seconds

References

[1] Chaoran Jiang et al. "Photoelectrochemical devices for solar water splitting–materials and challenges". In: *Chemical Society Reviews* 46.15 (2017), pp. 4645–4660.

[2] Suresh Kumar Kailasa, Kuang-Hung Cheng, and Hui-Fen Wu. "Semiconductor nanomaterials-based fluorescence spectroscopic and matrix-assisted laser desorption/ionization (MALDI) mass spectrometric approaches to proteome analysis". In: *Materials* 6.12 (2013), pp. 5763–5795.

[3] Daniel Loss and David P DiVincenzo. "Quantum computation with quantum dots". In: *Physical Review A* 57.1 (1998), p. 120.

[4] Jan Fischer, Björn Trauzettel, and Daniel Loss. "Hyperfine interaction and electron-spin decoherence in graphene and carbon nanotube quantum dots". In: *Physical Review B* 80.15 (2009), p. 155401.

[5] Michael H Kolodrubetz and Jason R Petta. "Coherent holes in a semiconductor quantum dot". In: *Science* 325.5936 (2009), pp. 42–43.

[6] Ning Wu, Daeyeon Lee, and Alberto Striolo. *Anisotropic Particle Assemblies: Synthesis, Assembly, Modeling, and Applications*. Elsevier, 2018.

[7] Raisei Mizokuchi. "Low-dimensional silicon-germanium heterostructures for quantum spintronics". PhD thesis. Université Grenoble Alpes, 2018.

[8] J Fick. "Crystalline nanoparticles in glasses for optical applications". In: *Handbook of Surfaces and Interfaces of Materials*. Elsevier, 2001, pp. 311–350.

[9] Floris A Zwanenburg et al. "Spin states of the first four holes in a silicon nanowire quantum dot". In: *Nano letters* 9.3 (2009), pp. 1071–1079.

[10] Bahram Ganjipour et al. "Transport studies of electron-hole and spin-orbit interaction in GaSb/InAsSb core-shell nanowire quantum dots". In: *Physical Review B* 91.16 (2015), p. 161301.

[11] Pei-Wen Li et al. "Study of tunneling currents through germanium quantum-dot single-hole and-electron transistors". In: *Applied physics letters* 88.21 (2006), p. 213117.

[12] O Klochan et al. "Fabrication and characterization of an induced GaAs single hole transistor". In: *Applied Physics Letters* 96.9 (2010), p. 092103.

[13] Sven Dorsch et al. "Gate control, g-factors and spin orbit energy of p-type GaSb nanowire quantum dot devices". In: *arXiv preprint arXiv:2103.15700* (2021).

[14] Bahram Ganjipour et al. "GaSb nanowire single-hole transistor". In: *Applied Physics Letters* 99.26 (2011), p. 262104.

[15] Carina Fasth et al. "Direct measurement of the spin-orbit interaction in a two-electron InAs nanowire quantum dot". In: *Physical review letters* 98.26 (2007), p. 266801.

[16] Philip Hofmann. *Solid state physics: an introduction*. John Wiley & Sons, 2015.

[17] Charles Kittel, Paul McEuen, and Paul McEuen. *Introduction to solid state physics*. Vol. 8. Wiley New York, 1996.

[18] John H Davies. *The physics of low-dimensional semiconductors: an introduction*. Cambridge university press, 1998.

[19] Anil Kumar, Geetam Richhariya, and Atul Sharma. "Solar photovoltaic technology and its sustainability". In: *Energy sustainability through green energy*. Springer, 2015, pp. 3–25.

[20] Walter A Harrison. *Solid state theory*. Courier Corporation, 1980.

[21] Thomas Ihn. *Semiconductor Nanostructures: Quantum states and electronic transport*. Oxford university press, 2010.
[22] Simon Min Sze. *Semiconductor devices: physics and technology*. John wiley & sons, 2008.
[23] Gilles Horowitz. "Drift-diffusion current in organic diodes". In: *arXiv preprint arXiv:1702.05674* (2017).
[24] Thomas F Kuech. "III-V compound semiconductors: Growth and structures". In: *Progress in Crystal Growth and Characterization of Materials* 62.2 (2016), pp. 352–370.
[25] AW Bett et al. "III-V compounds for solar cell applications". In: *Applied Physics A* 69.2 (1999), pp. 119–129.
[26] Rüdiger Paschotta et al. *Encyclopedia of laser physics and technology*. Vol. 1. Wiley Online Library, 2008.
[27] Matija Karalic et al. "Gate-tunable electronic transport in p-type GaSb quantum wells". In: *Physical Review B* 99.11 (2019), p. 115435.
[28] RC Ashoori. "Electrons in artificial atoms". In: *Nature* 379.6564 (1996), pp. 413–419.
[29] Kastner M.A. "Artificial atoms". In: *Physics Today* 46 (1993), pp. 24–31.
[30] Oliver Bierwagen. "Growth and anisotropic transport properties of self-assembled InAs nanostructures in InP". In: (2007).
[31] Ronald Hanson et al. "Spins in few-electron quantum dots". In: *Reviews of modern physics* 79.4 (2007), p. 1217.
[32] Leo P Kouwenhoven et al. "Electron transport in quantum dots". In: *Mesoscopic electron transport*. Springer, 1997, pp. 105–214.
[33] Carlo WJ Beenakker. "Theory of Coulomb-blockade oscillations in the conductance of a quantum dot". In: *Physical Review B* 44.4 (1991), p. 1646.
[34] T Ihn et al. "Graphene single-electron transistors". In: *Materials today* 13.3 (2010), pp. 44–50.
[35] Andreas Fuhrer. "Phase coherence, orbital and spin states in quantum rings". PhD thesis. ETH Zurich, 2003.
[36] Anne Thorne, Ulf Litzén, and Sveneric Johansson. *Spectrophysics: principles and applications*. Springer Science & Business Media, 1999.
[37] Christopher J Foot et al. *Atomic physics*. Vol. 7. Oxford University Press, 2005.
[38] Paul Ewart. *Atomic physics*. Morgan & Claypool Publishers, 2019.
[39] Chris C Escott, Floris A Zwanenburg, and Andrea Morello. "Resonant tunnelling features in quantum dots". In: *Nanotechnology* 21.27 (2010), p. 274018.
[40] Marcus Larsson et al. "g-factor and exchange energy in a few-electron lateral InGaAs quantum dot". In: *Applied physics letters* 95.19 (2009), p. 192112.
[41] Mikael T Björk et al. "Tunable effective g factor in InAs nanowire quantum dots". In: *Physical Review B* 72.20 (2005), p. 201307.
[42] *Triton*^{TM}200/400. Oxford Instruments Plc. 2012.
[43] Wilfred G Van der Wiel et al. "Electron transport through double quantum dots". In: *Reviews of Modern Physics* 75.1 (2002), p. 1.
[44] M Bhattacharya. "How to detect level crossings without looking at the spectrum". In: *American Journal of Physics* 75.10 (2007), pp. 942–946.
[45] FA Zwanenburg et al. "Ultrasmall silicon quantum dots". In: *Journal of Applied Physics* 105.12 (2009), p. 124314.

[46] I Van Weperen et al. “Spin-orbit interaction in InSb nanowires”. In: *Physical Review B* 91.20 (2015), p. 201413.

[47] S Nadj-Perge et al. “Spin–orbit qubit in a semiconductor nanowire”. In: *Nature* 468.7327 (2010), pp. 1084–1087.

[48] Christian Flindt, Anders S Sørensen, and Karsten Flensberg. “Spin-orbit mediated control of spin qubits”. In: *Physical review letters* 97.24 (2006), p. 240501.